

1 Impact of boundary layer stability on urban park
2 cooling effect intensity

3

4 *Authors: Martial Haeffelin¹, Jean-François Ribaud², Jonnathan Céspedes², Jean-*
5 *Charles Dupont³, Aude Lemonsu⁴, Valéry Masson⁴, Tim Nagel⁴, Simone Kotthaus²*

6

7 ¹ *Institut Pierre Simon Laplace (IPSL), CNRS, Ecole polytechnique, Institut Polytechnique de Paris, 91128*
8 *Palaiseau Cedex, France*

9 ² *Laboratoire de Météorologie Dynamique (LMD-IPSL), Ecole polytechnique, Institut Polytechnique de*
10 *Paris, 91128 Palaiseau Cedex, France*

11 ³ *Institut Pierre Simon Laplace (IPSL), Université Versailles Saint-Quentin-en-Yvelines, 78240*
12 *Guyancourt, France*

13 ⁴ *Centre national de recherches météorologiques (CNRM), Université de Toulouse, Météo-France,*
14 *CNRS, Toulouse, France*

15

16 Correspondence to: Martial Haeffelin (martial.haeffelin@ipsl.fr)

17 Abstract

18 The added heat in cities amplifies the health risks of heat waves. At night under calm winds
19 and cloud free skies, the air in the urban canopy layer can be several degrees warmer than in
20 rural areas. This lower nocturnal cooling in the built-up settings poses severe health risks to
21 the urban inhabitants as indoor spaces cannot be ventilated effectively. With heat waves
22 becoming more frequent and more intense in future climates, many cities are expanding their
23 green spaces with the aim to introduce cooling through shading, evaporation, and lower heat
24 storage capacities. In this study, it is assessed how the evening and night-time cooling effect
25 of urban parks (relative to nearby built-up settings) varies with the park size and the meso-
26 scale atmospheric conditions during warm summer periods. Using a combination of
27 meteorological surface station data and compact radiosondes, the cooling effect is quantified
28 for several urban parks (about 15 ha) and urban woods (about 900 ha). A profiling Doppler
29 wind lidar deployed in the city centre is used to measure turbulent vertical mixing conditions
30 in the urban boundary layer. We find that the maximum nocturnal cooling effects in urban
31 parks range around 1-5°C during a one-week heat wave event in mid-July 2022 but also in
32 general during summer 2022 (June-August). Three atmospheric stability and mixing regimes
33 are identified that explain the night-to-night variability in park cooling effect. We find that
34 very low turbulent vertical mixing in the urban boundary layer ($< 0.05 \text{ m}^2\text{s}^{-2}$) results in the
35 strongest evening cooling in both rural settings and urban parks and the weakest cooling in
36 the built-up environment. This regime specifically occurs during heat waves in connection
37 with large-scale advection of hot air over the region and corresponding subsidence. When
38 nocturnal turbulent vertical mixing above the city is stronger, the evening cooling in urban
39 green spaces is less efficient so that the atmospheric stratification above both urban parks
40 and woods is less stable and temperature contrasts compared to the built-up environment
41 are less pronounced. These results highlight that urban green spaces have a significant cooling
42 potential during heat waves, with maximum effects at night as advection and mixing transport
43 processes are minimal. This suggests adapting the opening hours of public parks to enable
44 residents to benefit from these cooling islands.

45

46 1 - Introduction

47 Excess heat in cities has impacts on human comfort, labour productivity, and health. Mortality
48 has been linked to exceptionally high temperatures during summertime heat waves both at
49 night and during the day (Basu et al. 2002; Keatinge et al. 2000; Pirard et al. 2005). During the
50 day, it is the outdoor radiative temperature that poses the most significant health risk. At
51 night, indoor temperatures are particularly important as people need to rest and indoor air
52 must be vented to cool the building for the upcoming day. However, urban inhabitants can
53 be particularly exposed to excessive and prolonged heat stress at night as the city and the
54 buildings do not cool efficiently, preventing necessary nocturnal rest. Hot nights following hot
55 days have been shown to make an important contribution to heat-related mortality (Murage
56 et al. 2017; Royé et al., 2021).

57

58 Reducing people's exposure to heat in cities can be addressed through urban planning
59 strategies. Increasing the vegetation fraction of urban areas is a widely accepted strategy to
60 mitigate urban heat risk by effectively reducing heat storage uptake during daytime
61 (Grimmond and Oke, 2002). Trees can provide efficient shading, reducing daytime air
62 temperatures by several degrees below their canopy, while evapotranspirative cooling
63 provided by vegetation, including trees, shrubs and grass, maintain the green space
64 temperature several degrees below that of the built-up environment (Shashua-Bar and
65 Hoffman, 2000). Green infrastructures also show cooling effects at night, through continued
66 evapotranspiration after sunset, generally larger sky-view factors in urban parks than in built-
67 up environments, and lower heat capacities. However, reduced radiative cooling and
68 ventilation can retain heat below the canopy at night (Taha et al. 1991).

69

70 The cooling effect intensity of urban green infrastructure has been shown to be highly variable
71 (Bowler et al. 2010; Shoulika et al 2014). Doick et al (2014) point to a lack of certainty on the
72 variables that drive the park cooling effects and on the multiple roles of trees and
73 greenspaces. Spatial contrasts in nocturnal temperatures between green infrastructure and
74 nearby built-up areas depend on park perimeter and area (Gao et al. 2022; Cai et al. 2023),
75 on proportion of grass and trees, on tree size (Zhu et al. 2021), on vegetation types and
76 arrangements (street trees vs parks), on density of vegetation (Holmer et al 2013), on park

77 topography (Barradas 1991; Chang et al. 2007), and on local climates (Ibsen et al. 2021). Other
78 authors investigated the spatial extent of cooling by urban parks, i.e. the *cooling effect*
79 *distance*, showing that it depends on both park size and park greenness (e.g. Zhu et al 2021).
80 From a recent review of park cooling effect studies conducted by Aram et al. (2019), we
81 conclude that most studies focus on the impact of park characteristics and investigations on
82 the impact of meteorological conditions on park cooling effects are rare.

83

84 The impact of meteorological conditions, such as cloudiness, wind and turbulence on
85 differential cooling is studied mostly at regional scale in terms of their impact on the urban
86 heat island (UHI) intensity (Oke 2017). While the influence of cloud cover and wind is rather
87 established (e.g. Morris et al. 2001, Lin et al. 2022), also the occurrence and characteristics of
88 night-time low-level jets are found to influence UHI intensity (Lemonsu et al. 2009; Cespedes
89 et al. 2024). However, the impact of local- to meso-scale meteorological phenomena on
90 cooling effects of urban green infrastructure is not well quantified.

91

92 The combined effects of green infrastructure characteristics and meteorological regimes on
93 nocturnal cooling must hence be better understood so that the cooling effect of urban
94 renaturation projects can be quantified more precisely. Which conditions affect the park
95 cooling effect intensity? What is the relative impact of park characteristics and meteorological
96 processes in the urban boundary layer on the cooling intensity ?

97

98 The overall objective of this study is to quantify in detail the nocturnal cooling effects of urban
99 parks during warm summertime conditions, taking into account potential cooling effects from
100 the rural surroundings. We carried out this study in the framework of the Heat and Health in
101 Cities project (H2C, Lemonsu et al. 2024) that focuses on the effects of excessive summertime
102 heat and air pollution on human vulnerability (Forceville et al. 2024) with the Paris region
103 (France) as a study area. A dedicated field campaign was designed and carried out in the city
104 of Paris and the surrounding region to monitor spatial and temporal variations in key
105 atmospheric thermodynamic variables in the urban canopy layer and urban boundary layer
106 during summer 2022. The measurements performed, including near-surface and vertical
107 profiles of temperature, humidity, wind and turbulence, and data analysis methodology are
108 presented in Section 2. Section 3 presents the analysis of urban park cooling effects in relation

109 to regional UHI and their variability during summer 2022, with a focus on a one-week heat
110 wave event. Next (Section 4), we investigate the characteristics of the urban boundary layer
111 structure under three distinct atmospheric turbulence regimes and their influence on park
112 cooling effects. Finally, we quantify the role of atmospheric stability and vertical turbulent
113 mixing on differential evening cooling between built-up locations, urban parks and rural
114 settings (Section 5).

115

116 2 - Data and methodologies

117 The present study is based upon data collected in the Paris region during the first Special
118 Observation Period of the Heat and Health in Cities project (SOP 2022, Figure 1), which was
119 conducted during summer 2022 (Lemonsu et al., 2024ab). This campaign also benefited from
120 measurements carried out in the context of other research initiatives such as the Paris 2024
121 Olympics WMO Research and Development Project (RDP-2024) and the ACTRIS research
122 infrastructure (Laj et al. 2024). This multi-project context motivated the pooling of resources,
123 a coordinated strategy for the organisation of the summer-2022 experimental campaigns, and
124 the development of a joint data repository under the name PANAME (PARis region urbaN
125 Atmospheric observations and models for Multidisciplinary rEsearch - see
126 <https://paname.aeris-data.fr/>).

127

128 2.1 Datasets used in the study

129 This study combines continuous measurements collected from June to August 2022 and 14
130 one-day intensive observation periods (IOPs), with data collected from mid-June to the end
131 of July 2022. Measurement locations are shown in Figure 1.

132

133 i) Surface meteorological stations

134 Météo France's operational network consists of some fifty ground-based weather stations in
135 the Paris region measuring at least air temperature at 2 m AGL with a 6-minute acquisition
136 time step. A few stations provide additional meteorological parameters such as wind speed
137 and direction at 10 m AGL, global incoming radiation, precipitation, and cloud cover. The

138 stations are spread across the region in different areas, but are always installed on the ground
139 on an open lawn (according to WMO recommendations).

140

141 We selected six stations to represent rural settings (Local Climate Zone, Stewart and Oke
142 2012) of the Paris region (Figure 1), located in Changis, Courdimanche, Fresnoy-La-Riviere,
143 Maule, Melun, and Pontoise, which is similar to the stations selected by Lemonsu et al. (2015).
144 The stations are geographically distributed in all directions relative to the city centre of Paris
145 and located at altitudes ranging 50-90 m above sea level (ASL). In our study, the reference
146 rural setting conditions of temperature, wind speed and direction are computed as the
147 average of the variables measured at those six stations (Changis, Courdimanche, Melun, and
148 Pontoise stations).

149

150 Near-surface urban park weather conditions are documented by a Météo-France weather
151 station located in the Montsouris Park, a 15-ha park located in the 14th district, south of the
152 Paris city centre. The station, located at an elevation of 75 m ASL, provides 2-m air
153 temperature and humidity measurements. Wind speed and direction are measured at 25 m
154 above ground level (AGL). A detailed description of temperature measurements in the
155 Montsouris Park is provided by Dahech et al. (2020).

156

157 The Paris built-up setting conditions are sampled using Internet of Things (IoT) temperature
158 and humidity measurements. This compact technology opens up new perspectives in
159 meteorological measurements, particularly in urban environments where measurement and
160 installation conditions are sometimes complicated. More than twenty IoT stations (DecentLab
161 DL-SHT35-001 - air temperature and humidity sensor with radiation shield for LoRaWAN) have
162 been installed in central Paris starting in July 2022. These are compact and lightweight
163 stations installed on lampposts at a height of approximately 5 m AGL, following the
164 recommendations made by Oke (2006). The stations have been installed on the north side of
165 the lampposts to limit sensor warming through solar irradiance. The reference built-up setting
166 temperature is computed as the average temperature recorded by four IoT stations located
167 within 500 m of each other, in the highly urbanised neighbourhood of the Paris Opera House
168 (hereafter referred to as Opera). Note that these stations were operational only from July 8,
169 2022. For the period prior to this date (1 June to 7 July), the built-up setting temperature is

170 derived from the Météo France weather station Lariboisière Hospital (10th district of Paris)
171 which is located 2 km northeast of the Opera neighbourhood in an equally dense built-up
172 setting. Comparisons of temperatures measured at Lariboisière and Opera during July and
173 August 2022 do not reveal any significant differences (not shown). The built-up setting
174 temperature (at Lariboisière and Opera) is considered not influenced by green space cooling,
175 as the closest urban park is about 1 km away and cooling effect distances of parks reported
176 in the literature are far less than 1 km (Aram et al. 2019).

177

178 Finally, we used temperature and wind speed and direction measured at the top of the Eiffel
179 Tower (287 m AGL) to monitor conditions at a height generally located in the nocturnal urban
180 boundary layer.

181

182 **i) Doppler Wind Lidar**

183 A Doppler Wind Lidar (DWL) is used in this study to deduce the intensity of vertical turbulent
184 mixing. The Vaisala DWL WindCube Scan 400 was installed at 90 m above ground level (AGL)
185 at the top of the Zamansky Tower located on the campus of Sorbonne University in the 5th
186 district of Paris (QUALAIR atmospheric station location shown on Fig. 1; <https://qualair.fr/>) to
187 measure horizontal wind and vertical velocity. In this study, we use vertical-stare mode of the
188 DWL to derive vertical velocity variance (σ_w) profiles. Each variance profile is calculated from
189 300 vertical velocity profiles collected during a 5-min period (one profile per second). Vertical
190 velocity variance profiles are available every 30 minutes. Due to the installation setup, the
191 first gate available for deriving the vertical velocity variance is at 240 m AGL.

192

193 **ii) Windsond**

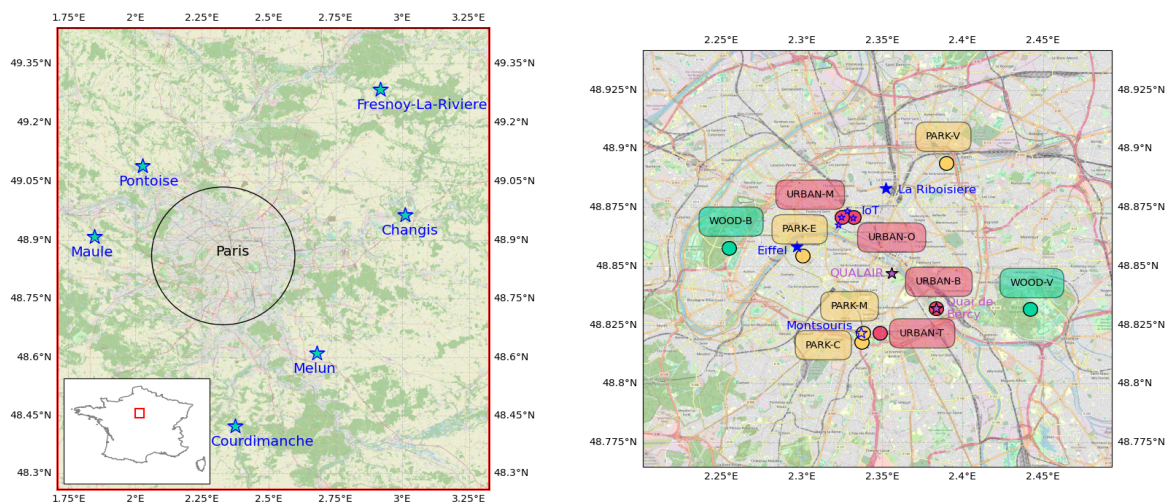
194 A Windsond is a lightweight sonde (12 grams) manufactured by Sparv Embedded, Sweden
195 (<https://sparvembedded.com/products/windsond>). This instrument, packaged in a styrofoam
196 cup, records pressure, temperature, and relative humidity approximately every second.
197 Latitude and longitude are determined using an onboard GPS receiver. The S1H3 windsond
198 model calculates wind speed and direction independently from latitude and longitude,
199 utilising the GPS signal. Thanks to its lightweight design, the balloon size is somewhat

200 equivalent to a "party balloon", requiring about 50 L of helium, and making it particularly
201 suitable for probing the lower parts of the troposphere.

202 For each IOP, three profiles were produced using windsonds to monitor evening cooling at
203 16, 20 and 00 UTC. The 16 UTC profile corresponds to conditions of maximum daytime
204 temperatures. The 20 UTC profile samples conditions about 1 hr after sunset, while the 00
205 UTC profile is performed in conditions close to the maximum nighttime UHI.

206 Corrections have been applied to raw data as follows. Before the windsond is released, the
207 temperature and humidity sensors are not ventilated. Unventilated data (before launch) are
208 thus carefully compared with the first points of the ventilated profile, and corrected if
209 necessary. As the temperature and humidity sensors are outside the styrofoam cup, the
210 windsond is subject to the influence of solar radiation during the day. A daytime overheating
211 on the order of about +1°C was observed by comparing those profiles with data collected by
212 Vaisala RS41-SGP radiosondes launched at the same time the URBAN-B location (see
213 Appendix 1). A correction of -1°C was therefore applied across the entire profile for
214 windsonde data at 16 UTC. No radiative correction is applied at 20 and 00 UTC.

215



216
217 Figure 1: (left) Locations of the six weather stations contributing to the rural setting
218 reference. (right) Locations of fixed weather stations in Paris city (blue stars) and of
219 windsonde and radiosonde launch sites in urban woods (green dots WOOD), urban
220 parks (yellow dots PARK) and built-up areas (red dots URBAN). © OpenStreetMap
221 contributors 2023. Distributed under the Open Data Commons Open Database
222 License (ODbL) v1.0.

223

224
225

226 2.2 Sampling methodology

227

228 Our study focuses on evening temperature evolution at various locations across the Paris
229 region under predominantly cloud free conditions. The cloud cover fraction is derived on an
230 hourly basis using a Lufft CHM15k automatic lidar ceilometer located at the SIRTA observatory
231 (Haeffelin et al. 2005) and a second one located at the QUALAIR atmospheric station. Evening
232 cloud-free conditions are defined as a cloud fraction less than 20% for each hour between 16
233 and 00 UTC. In the period June-August 2022, 54 days are classified as “evening cloud-free
234 conditions”. On average this period is characterized by a positive temperature anomaly and
235 near-zero precipitation anomaly (not shown).

236

237 The 14 intensive observation days were selected to focus predominantly on warm to hot
238 daytime conditions followed by cloud free nights. Two heat wave events were covered with
239 intensive observations, the first one on 16-18 June and the second one on 12-19 July.

240 Windsong launch sites were classified in three types of settings i.e., urban woods, urban parks
241 and built-up areas. Two urban woods, located East of the city (Bois de Vincennes, 995 ha;
242 WOOD-V in Fig. 1) and West of the city (Bois de Boulogne, 845 ha; WOOD-B), are mostly
243 wooded, including open lawns, small lakes, buildings and roads. Three urban parks of
244 comparable size were selected to sample different neighbourhoods of the city. One is located
245 south of the city centre (Cité Universitaire about 32 ha with 50% green space and 50%
246 housings and small roads, located across the street from Montsouris Park; PARK-C), the
247 second one is West of the city centre (Eiffel Tower park, 24 ha, predominantly trees and open
248 lawns; PARK-E), and the third one is Northeast of the city centre (La Villette Park, 55 ha
249 including 30 ha of green space and 25 ha of built-up areas; PARK-V). The three selected urban
250 parks differ however in terms of vegetation type (species; fractions of trees, shrubs and grass)
251 and also in terms of irrigation practices and hence soil moisture. These differences and their
252 effects are not accounted for in this study. Windsongs were also launched from four built-up
253 areas: one in the 13th district close to Montsouris Park (URBAN-T in Fig 1.), two in the 9th
254 district close to the Opera IoT stations (URBAN-M and URBAN-O), and one in the 12th district

277 sites - see detailed definition of locations in Section 2). As park cooling effect intensity is
278 reported to be highly variable, we study this variability as a function of the nocturnal UHI in
279 the Paris region, which represents the regional-scale temperature contrasts between the
280 same built-up environment and the vegetated rural reference. The study covers summer 2022
281 focusing on the 54 evening periods with cloud-free conditions (defined in Section 2).
282

283 3.1 Summertime urban park cooling effect variability

284 The regional UHI is known to be dependent on both cloud-cover fraction and wind speed.
285 Here we focus on cloud-free nights, for which the UHI has been found to be proportional to
286 the inverse of the square-to-third root of the wind speed (e.g. Morris et al. 2001). Cespedes
287 et al. (2024) has also shown that the strongest UHI intensities are found for very low vertical
288 velocity variance values, measured above the urban canopy, and that UHI decreases as
289 vertical velocity variance increases.

290 Fig. 2 presents median nocturnal cooling intensity of the Montsouris Park (a 15-ha urban park)
291 against the median nocturnal regional UHI and median vertical velocity variance computed
292 over the 19-02 UTC time interval for each night. A K-means clustering method based on the
293 three variables is used to identify different regimes. The figure reveals three different
294 regimes. In conditions of strongest UHI (6-10°C), we find a group of days where the park
295 cooling effect intensity ranges 2-5°C. In this regime, the vertical velocity variance is very low
296 with median nocturnal values ranging from 0.02 to 0.1 m²s⁻². In these conditions, urban park
297 cooling intensity relative to the built-up environment shows a strong variability, but is on
298 average half the regional UHI intensity. In conditions of weak UHI intensity (2-4°C), the park
299 cooling effect is close to 1°C, while the vertical velocity variances are high (greater than 0.25
300 m²s⁻²). In this regime, intra-urban temperatures are most homogeneous and urban-rural
301 contrasts are minimal, which is likely due to significant advection. In between, we find a
302 number of days where the urban park cooling effect remains limited (1-2°C), while the urban-
303 rural temperature contrasts are significantly stronger (4-8°C), by a factor of about four. In
304 these conditions, we find that the vertical velocity variances range between 0.1 and 0.2 m²s⁻²
305 ². For those days, the rural environment around the city cools very efficiently, while the urban
306 setting remains hot with little intra-urban contrasts.

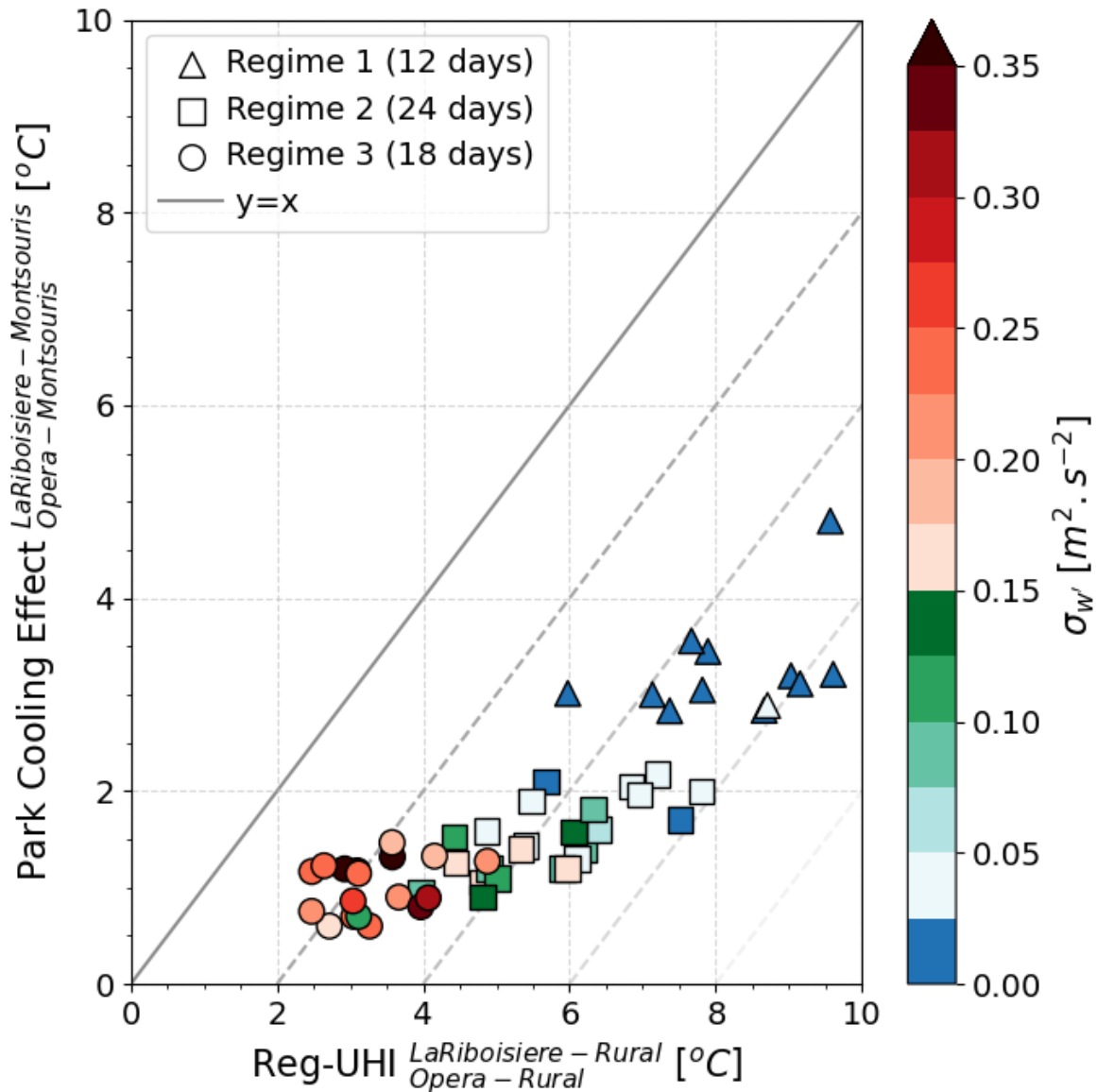
307 In summary, we can state that:

- 308 ● Conditions of strong park cooling intensity combined with strong regional UHI
309 intensity occur in a regime of low vertical velocity variance. This regime will be referred
310 to as the stagnant regime in the rest of the paper,
- 311 ● Conditions of moderate park cooling intensity combined with strong regional UHI
312 intensity occur in a regime of moderate vertical velocity variance (referred to as the
313 intermediary regime).
- 314 ● conditions of weak park cooling intensity combined with weak regional UHI intensity
315 occur in a regime of high vertical velocity variance (referred to as the turbulent
316 regime).

317 Based on these findings, several questions arise. What processes drive the evening cooling in
318 the urban park in these different conditions? What is responsible for the different urban park
319 cooling effects that we find for low, moderate and high vertical velocity variance?

320

321



322

323 Figure 2. Nocturnal urban park cooling effect intensity against regional-scale UHI intensity and
 324 vertical velocity variance (color scale), derived from 8 hours of measurements (median 19-02
 325 UTC values) for the 54 cloud-free evenings.

326

327 3.2 Urban park cooling effect variability in a heatwave period

328

329 To better understand factors affecting the variability in nocturnal temperature contrasts
 330 between urban parks and the built-up settings, we focus next on an eight-day event (12-19

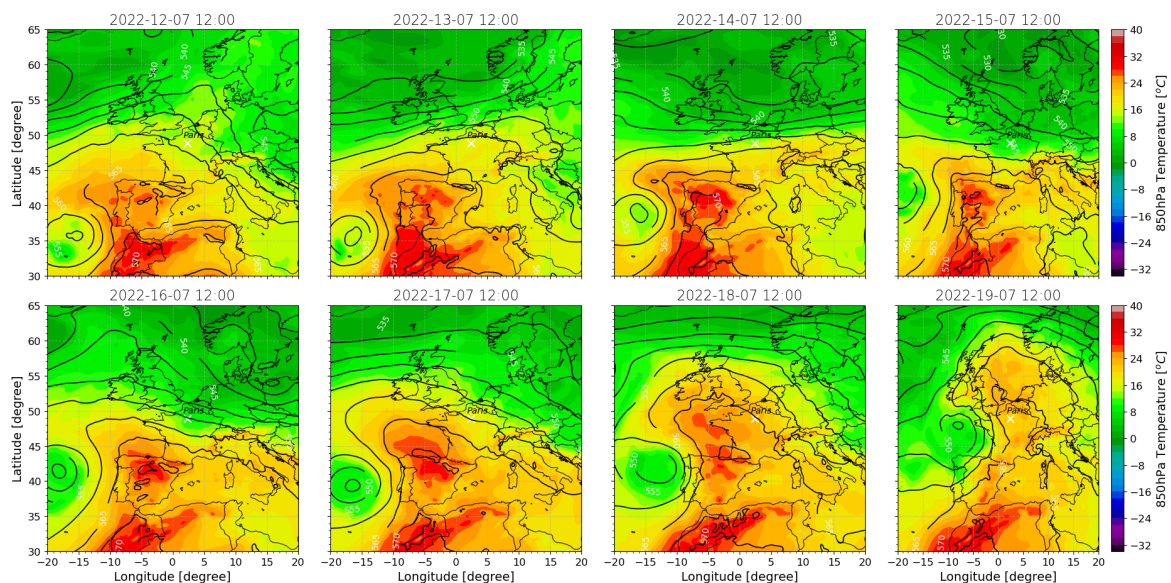
331 July 2022) that is characterised by extreme daytime temperature (peak values approaching
332 40°C on several days) and a set of diverse evening cooling patterns.

333

334 This period is characterised by a powerful anticyclonic axis between Morocco, France and the
335 British Isles, which gradually warmed the air (Fig. 3). A secondary low-pressure system located
336 between the Azores and Portugal moved towards the Bay of Biscay, strengthening advection
337 of particularly hot air from the Iberian Peninsula. This contributed to the intensification of a
338 heatwave over the European continent, with an extreme peak over the Paris region on 19
339 July. As it moved north-eastwards over France, this low pressure system advected cooler
340 oceanic air from the west, causing temperatures to fall and progressing eastwards with
341 thunderstorm activity. During the heatwave, the 850 hPa temperature exceeded 20°C, while
342 on standard summer days, it is closer to 10°C.

343

344



345

346 Figure 3: Synoptic overview from 12 to 19 July 2022 based on ERA5 reanalysis. The colour
347 bar represents temperature at 850 hPa, and the contours represent the geopotential height
348 difference between 500 hPa and 1000 hPa (dam).

349

350 Figure 4 shows the temporal evolution of near-surface atmospheric conditions during the
351 eight-day period. Figure 4a compares the 2-m air temperature measured in Opera built-up
352 setting, Montsouris urban park, and the rural reference setting. The regimes identified in
353 Section 3.1 are also shown for each night. Figure 4b presents the rate of change of

354 temperature over time at the three locations. Figure 4c shows the temperature differences
355 between the built-up site and the urban park and the rural setting, respectively. Figure 4d
356 presents the wind speed and direction measured at the Montsouris urban park 25 m AGL and
357 Fig. 4e shows the vertical velocity variance measured at 240 m AGL.

358

359 The eight-day period is characterised by a first heat wave on July 12 and 13 (stagnant regime),
360 due to the advection of hot air shown in Fig. 3, with maximum temperature exceeding 35°C,
361 followed by three days of more moderate heat on July 14, 15, and 16 (intermediary and
362 turbulent regimes, maximum temperature at or below 30°C and minimal temperatures in the
363 built-up environment less than 20°C). A second, more intense, advection of hot air occurs the
364 following three days on July 17, 18, and 19 (stagnant regime) with daytime maximum
365 temperatures exceeding 35°C. Figure 4a shows that the daytime maximum temperatures
366 (between 16 and 17 UTC) in the built-up, urban park and rural settings are close, within 1°C
367 of each other. Conversely, night-time minimal temperatures (between 03 and 04 UTC) differ
368 by 4-10°C between the built-up and rural settings with significant day to day variations (Figure
369 4c).

370

371 Figure 4b shows positive heating rates from sunrise until about one hour before sunset. Peak
372 heating rates reach 2-3°C/hr, but are on average near 1°C/hr. One hour before sunset,
373 temperature changes become negative (cooling). We observe a two-phase cooling consistent
374 with earlier findings reported in the literature (e.g. Holmer et al. 2013). The first phase lasts
375 from 16 to 21 UTC. It is characterised by large changes in cooling rate reaching maximum
376 values near 19-20 UTC and with differences of up to 2°C/hr between built-up, urban park, and
377 rural cooling rates (on 12/07, 17/07 and 18/07). The second phase starts after 21 UTC and
378 lasts until sunrise or about 04 UTC. It is characterised by more moderate cooling rates of
379 typically less than -1°C/hr and by virtually no contrasts between built-up, park and rural
380 settings.

381

382 In the evening, air temperature cooling in the urban canopy is driven by a combination of
383 processes, including radiative cooling of the surfaces and the air (through radiative flux
384 divergence), turbulent heat exchange (through sensible and latent heat fluxes), release of
385 heat from the ground (storage heat flux), vertical mixing of air, and advection (Oke 2017).

386 These processes are known to depend on the surface types and properties (albedo, emissivity,
387 heat capacity, soil moisture), the 3-D canopy structure (sky view factor), the city morphology,
388 anthropogenic heat emissions, the spatial distribution of surface types (urban to rural surface
389 gradients), and synoptic-scale weather conditions (wind, clouds). According to Steeneveld et
390 al. (2006), atmospheric static stability and mesoscale dynamics affect the relative contribution
391 of the radiative and turbulent processes. When the vertical turbulent mixing is low, turbulent
392 heat fluxes are weak, hence air temperature cooling is dominated by radiative flux divergence,
393 partially compensated by the storage heat flux.

394

395 This is consistent with cooling rates shown in Fig. 4b. In the rural setting and in the urban park,
396 where the storage heat flux is low, the largest cooling rates (peaking at $-3^{\circ}\text{C}/\text{hr}$ and $-2^{\circ}\text{C}/\text{hr}$
397 respectively) are observed in conditions of low vertical velocity variance (Fig. 4e), on the
398 evenings of 12/07, 17/07 and 18/07 (stagnant regime). In the built-up area, the radiative
399 cooling is partially compensated by a stronger ground heat flux. On nights with moderate to
400 high vertical velocity variance, radiative flux divergence is reduced and also compensated by
401 sensible and latent heat flux releases, which leads to lower cooling rates in both urban park
402 and rural settings. The excess of urban-park cooling compared to the built-up environment
403 lasts four to six hours (from 18 to 00 UTC) as is the case for the rural surface.

404

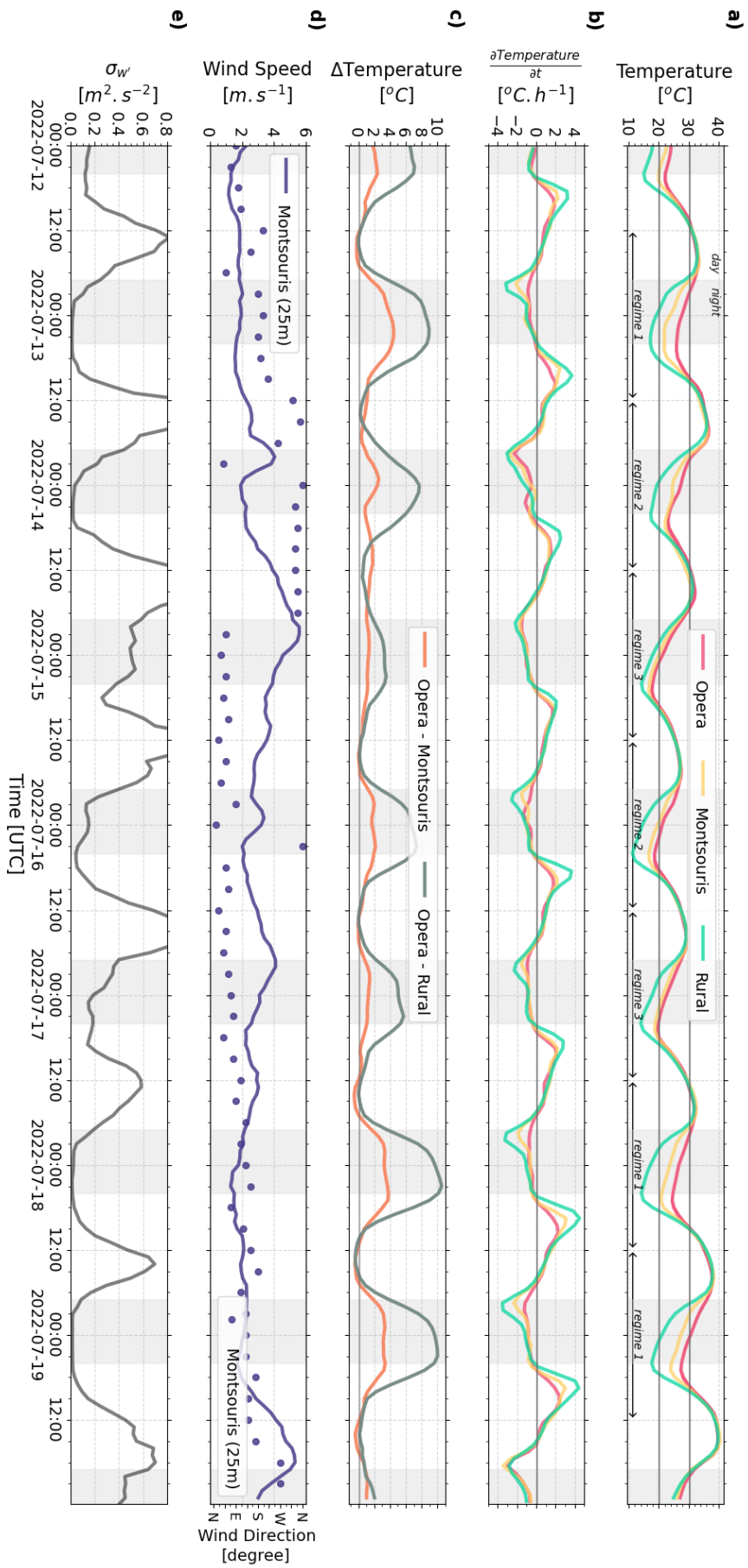
405 The contrasts in cooling rates between the built-up environment, the urban park and the rural
406 settings can explain the large variability in nocturnal park cooling effect and regional-scale
407 UHI intensities shown in Fig. 4c. On the three nights with lowest wind speed ($<2\text{ m s}^{-1}$, Fig. 4d)
408 and lowest vertical velocity variance ($<0.05\text{ m}^2\text{ s}^{-2}$), that is on 12-13/07, 17-18/07 and 18-
409 19/07 (stagnant regime), the maximum regional UHI intensity exceeds 8°C , while the
410 maximum park cooling effect reaches nearly 4°C . On those nights, in the built-up
411 environment, the air temperature cools by $7-9^{\circ}\text{C}$ from sunset to sunrise, while the urban park
412 cools an extra $3-4^{\circ}\text{C}$, and the rural setting an additional $3-4^{\circ}\text{C}$. On the night with moderate
413 wind speed ($3-4\text{ m s}^{-1}$) and moderate vertical velocity variance, 15-16/07(intermediary
414 regime), the regional UHI peaks near 6°C , while the park cooling effect reaches about 2°C . On
415 this night, the air temperature cools by about 10°C from sunset to sunrise in the built-up
416 environment, while the urban green infrastructure cools an extra 2°C , and the rural setting an
417 additional $3-4^{\circ}\text{C}$. On the nights of 14-15/07 and 16-17/07 (turbulent regime), the wind speed

418 exceeds 4 m s^{-1} and the park cooling effect reaches just 1°C , while the maximum regional UHI
419 intensity is about 4°C .

420

421 The analysis of the 12-19 July period confirms the results shown in Fig. 2. Different regimes
422 exist that influence park cooling effect and regional UHI intensities. In particular, during nights
423 with very low wind speeds, the air above the urban park cools significantly more (up to 4°C)
424 than in our reference built-up environment. To better understand the processes and
425 conditions that affect these nocturnal intra-urban cooling contrasts we will investigate the
426 dynamics and thermodynamics of the urban boundary layer over green infrastructures of
427 different sizes in the following section.

428



430 Figure 4: near-surface temperature and nighttime turbulence regimes (a) and cooling rate (b)
431 measured in a built-up environment (Paris Opera district), an urban park (Montsouris park,
432 15-ha), and the average of 6 rural locations around Paris; Urban park cooling effect (Opera-
433 Montsouris temperature difference) and regional-scale UHI (Opera-Rural temperature
434 difference) (c); wind speed and direction measured at Montsouris Park 25 m AGL (d); and
435 vertical velocity variance measured in Paris city centre 240 m AGL. 12-19 July 2022; during
436 that week, the sun sets at about 19 UTC and rises at about 04 UTC.
437

438 4) Evening cooling in and above urban parks and 439 urban woods

440
441 In this section, we focus on four different nights to study the characteristics of evening cooling
442 mechanisms above urban green spaces considering dynamics of the urban boundary layer for
443 the three turbulence regimes. For each evening period (16-00 UTC), we analyse time series of
444 near-surface temperature, humidity, and wind measured in the built-up environment, urban
445 green infrastructures, and rural settings. To investigate the relative role of relevant cooling
446 mechanisms, i.e. radiative cooling of the surfaces, radiative cooling of the air through
447 radiative flux divergence, turbulent heat exchange, vertical mixing, and advection, it is helpful
448 to quantify conditions in the urban boundary layer. Therefore, in order to assess the relative
449 roles of surface-driven and atmospheric-driven processes, the conditions measured at the
450 surface are complemented by the analysis of the observations at the top of the Eiffel Tower
451 (287 m AGL), as well as vertical profiles of meteorological variables obtained from windsound
452 profile measurements.
453

454 4.1 Stagnant regime: strong park cooling effect combined with 455 strong UHI intensity

456

457 Here we focus on two nights that show the strongest park cooling effect intensity and most
 458 significant UHI intensity, classified as stagnant regime, i.e. 12-13/07 and 17-18/07. Both
 459 selected nights occur in high-pressure synoptic conditions with meso-scale subsidence over
 460 the region. Hot air advection driven by a secondary pressure low located west of the Iberian
 461 Peninsula led to 850 hPa temperatures near 20°C. Both nights are characterised by very warm
 462 conditions over the preceding daytime period with daily maximum air temperatures
 463 exceeding 32°C (see Fig.s 5a, 6a). Strong regional-scale UHI and park cooling intensities are
 464 due to sharp contrasts in peak cooling rates (Fig.s 5b and 6b) between built-up, park and rural
 465 settings that last for 4-6 hours. On both 12/07 and 17/07, an evening cooling (16-00 UTC) of -
 466 5°C, -9°C and -14°C is documented in the built-up, urban park and rural settings, respectively,
 467 as shown in Table 2.

468

	16-00 UTC cumulative temperature change [°C] (average cooling rate [°C/h])		
Regimes	Opera	Park	Rural
Stagnant Regime : Strong park cooling effect and strong UHI intensities	-5.1 (-0.6)	-9.1 (-1.1)	-14.0 (-1.8)
Intermediary Regime: Moderate park cooling effect and strong UHI intensities	-5.9 (-0.7)	-7.6 (-0.9)	-12.6 (-1.6)
Turbulent Regime: Weak park cooling effect and low UHI intensities	-9.6 (-1.2)	-9.4 (-1.2)	-13.1 (-1.6)

469 Table 2: 16-00 UTC cumulative evening temperature change and average cooling rate for the
 470 three types of turbulence regimes.

471

472 The relatively strong cooling rate in the urban park compared to the built-up settings suggests
473 that the surface-driven processes (i.e. radiative cooling and/or turbulent latent heat fluxes)
474 are rather efficient on those nights. In comparison, the air temperature at the top of the Eiffel
475 Tower peaks generally around 18 UTC, i.e. about 2 hr later than near the surface at values 2-
476 3°C colder than the near-surface air temperature (Fig.s 5a and 6a). After 18 UTC, the air starts
477 to cool with a rate of around -0.35°C/hr, which is nearly half the value of the near-surface
478 cooling rate measured in the built-up environment (Fig.s 5b and 6b). Hence, the air at 287 m
479 AGL is only moderately affected by the processes that cool the air close to the surface. This is
480 the first evidence of decoupling between the urban canopy layer (UCL) and the air above, and
481 the decrease in static instability in the urban boundary layer (UBL).

482

483 Further evidence of this decoupling due to static stability in the UBL can be found in the wind
484 speed measurements. Figures 5c and 6c show the time series of wind speed at 10 m AGL at
485 the Melun rural site, at 25 m AGL in the Montsouris urban park and at 287 m AGL at the Eiffel
486 Tower, for 12/07 and 17/07, respectively. A comparable temporal evolution of wind speed
487 can be observed in the evening hours on both days. During the afternoon, the wind speed at
488 both the urban park and the rural site are consistent (about 2-4 m s⁻¹ and within 1-2 m s⁻¹ of
489 each other). After about 18 UTC, the wind speed at 287 m AGL increases rapidly to reach 8-
490 10 m s⁻¹ before 00 UTC, while the rural and urban park wind speed remains low at or below 2
491 m s⁻¹, i.e. often lower than during daytime. This is a second evidence that after sunset,
492 decoupling conditions occur between the surface layer and the air above.

493

494 Figures 5 and 6 g and h show vertical profiles of wind speed and direction derived from
495 windsound profiles launched at 16, 20 and 00 UTC over an urban park (PARK-E; Fig. 1) on 12/07
496 and a large urban wood (WOOD-B; Fig. 1) on 17/07, respectively. Both IOPs are characterised
497 by easterly winds with relatively little wind direction evolution in the evening. During daytime
498 (16 UTC), the wind speed is moderate (2-4 m s⁻¹) in the first 700 m of the atmospheric
499 boundary layer. The windsounds launched after sunset (near 20 UTC) reveal in both cases low
500 near-surface wind speed (1.5-2.0 m s⁻¹) that gradually increases with height (consistent with
501 results described in the previous paragraph). A 3 m s⁻¹ wind shear can be observed on 17/07
502 between the surface and 200 m AGL. The wind shear is not as strong on 12/07, possibly

503 because the profile was measured 45 min earlier than on the other day. This wind shear is a
504 signature of the stabilisation of the atmosphere that inhibits the vertical transfer of
505 momentum and hence decouples the air aloft from surface drag effects, allowing the wind
506 speed to increase aloft (e.g. Barthelemie et al. 1996).

507

508 The windsonds launched at 00 UTC reveal even stronger windshear between surface and 200
509 m AGL, with maximum wind speed of around 6.5 m s^{-1} on both nights near 300 m AGL and a
510 decreasing wind speed above. This vertical structure is known as a low-level jet (LLJ), a
511 condition that occurs frequently on summer nights above Paris according to Céspedes et al.
512 (2024). Their work has shown that very low altitude LLJs are associated with low levels of
513 turbulence, due to the fact that they form in a statically stable atmosphere that inhibits
514 mechanically induced turbulence.

515

516 To characterise the importance of vertical mixing as a potential means for heat transfer
517 between the UCL and the nocturnal urban boundary layer, we use Doppler wind lidar
518 measurements to derive time series of vertical velocity variance (Figs 5d and 6d). During the
519 convective period of the two IOPs, the vertical velocity variance typically exceeds $0.5 \text{ m}^2 \text{ s}^{-2}$. It
520 then decreases rapidly around sunset. At 20 UTC, the values have dropped to less than 0.05
521 $\text{m}^2 \text{ s}^{-2}$ on both 12/07 and 17/07, and remain very low all night. This confirms the very low
522 vertical turbulent mixing in the UBL on both nights. It should be noted that in the stagnant
523 regime, the vertical velocity variance values are very low (less than $0.05 \text{ m}^2 \text{ s}^{-2}$) throughout
524 the LLJ layer that extends from 240 to about 500 m AGL or more (not shown). Hence even
525 though vertical velocity variance is not constant with height and the measurement height
526 (240 m AGL) is close the top of the UBL, we conclude that the vertical velocity variance value
527 at 240 m AGL is representative of the nocturnal urban boundary layer turbulence regime.

528

529 To characterise the role of vertical radiative flux divergence in the atmospheric boundary
530 layer, and to better understand the relative importance of surface-driven vs atmospheric-
531 driven processes, we analyse the vertical structure of temperature and its temporal evolution.
532 In the Eiffel Tower urban park (PARK-E), we find that near-surface temperatures measured by
533 the windsond on 12/07 are consistent with temperatures recorded by the Montsouris urban
534 park surface station (yellow circles in Fig. 5a). At 20 UTC, we observe a 1°C temperature

535 inversion between the surface and 50 m AGL (Fig. 5f). Above the inversion, the temperature
536 decreases adiabatically by about $-1^{\circ}\text{C}/100\text{ m}$ so that the potential temperature is nearly
537 constant in a statically neutral layer between 50 and 700 m (Fig. 5f). At 00 UTC, the surface-
538 based inversion has become stronger ($\Delta T_{\text{air}} = 2.5^{\circ}\text{C}$ and $\Delta \theta_{\text{air}} = 3.0^{\circ}\text{C}$ between the surface and
539 50 m AGL), and two elevated inversions have formed near 100 and 200 m AGL (Fig. 5f, g), with
540 $\Delta \theta_{\text{air}} = 0.5^{\circ}\text{C}$ followed by a statically stable layer with a $+0.2^{\circ}\text{C}/100\text{ m}$ lapse rate (Fig. 5g).

541

542 In the urban wood (WOOD-B), near-surface temperatures measured by the windsond on
543 17/07 are close to temperatures measured in the rural settings (green circles in Fig. 6a). With
544 3.5°C decrease over 50 m, the surface-based temperature inversion at 20 UTC (Fig. 6e) is
545 already stronger than the inversion observed at 00 UTC over PARK-E on 12/07. Above the
546 inversion, the temperature decreases adiabatically (Fig. 6e, f) and the potential temperature
547 profile confirms that the stable wood UBL is capped by a neutral layer above. At 00 UTC, the
548 surface-based inversion strengthens and extends aloft ($\Delta T_{\text{air}} = 5.0^{\circ}\text{C}/100\text{ m}$; $\Delta \theta_{\text{air}} = 6^{\circ}\text{C}/100$
549 m), followed by an elevated inversion near 250 m AGL (Fig. 6f, g). The potential temperature
550 profile is stable between 100 and 300 m AGL ($+1.0^{\circ}\text{C}/100\text{ m}$) and moderately stable
551 ($+0.2^{\circ}\text{C}/100\text{ m}$) above (Fig. 6g).

552

553 These elevated inversions observed both over the urban park and urban wood could be
554 formed through localised radiative cooling, subsidence and/or advection of statically stable
555 rural air that is commonly observed above nocturnal UBL (e.g. Tsiringakis et al. 2022). Elevated
556 inversions in nocturnal UBLs are simulated and studied extensively in Martilli (2002). The drag
557 and turbulent kinetic energy production induced by the urban structure increases with
558 increasing wind speed. Vertical mixing of potential temperature leads to a local minimum of
559 temperature at the location of maximum turbulence through a negative turbulent heat flux.
560 According to Martilli (2002), the net result of the vertical turbulent transport is to heat the
561 layer below the base of the inversion and to cool the inversion layer. Cooling of the inversion
562 layer (roughly between 200 and 300 m AGL) is clearly seen on the both windsond temperature
563 profiles measured at 00 UTC.

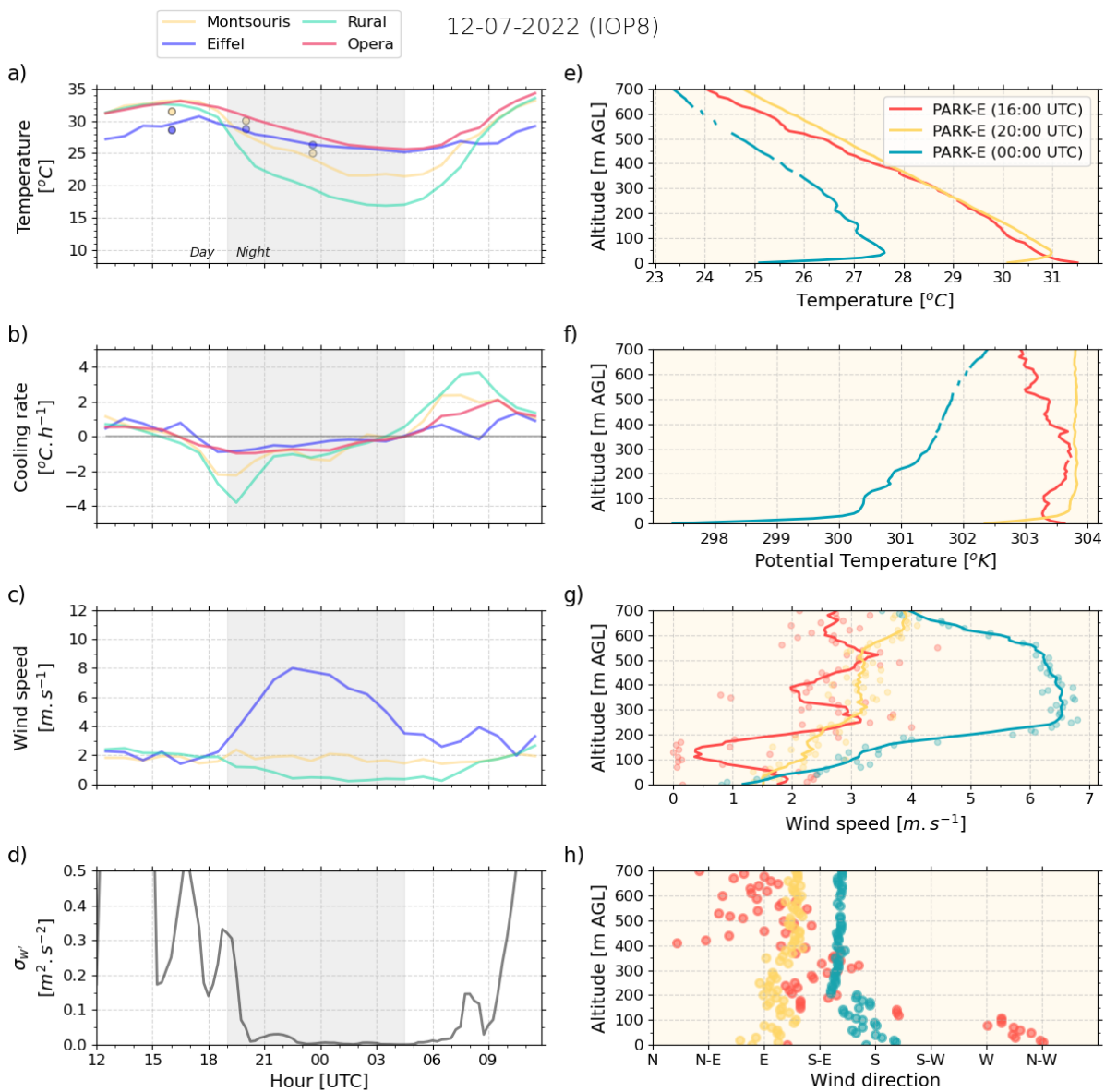
564

565 We can conclude that the conditions of stagnant regime, combining strong park cooling
566 effects and strong UHI intensities, are associated with a significant surface-based inversion

567 that leads to the decoupling not only of the rural nocturnal boundary layer from the residual
 568 layer but also between the urban boundary layer and the neutral layer above. The strong
 569 stratification suppresses nearly any turbulent vertical motion so that the UBL height is rather
 570 shallow - even below the top of the Eiffel Tower. As the flow is no longer subject to surface
 571 drag, a regional low-level jet forms that likely advects rural, statically stratified air over the
 572 UBL, which can influence the development of elevated inversions. The strong stratification in
 573 the park internal UBL is the result of cooling dominated by radiative flux divergence due to
 574 low turbulent mixing.

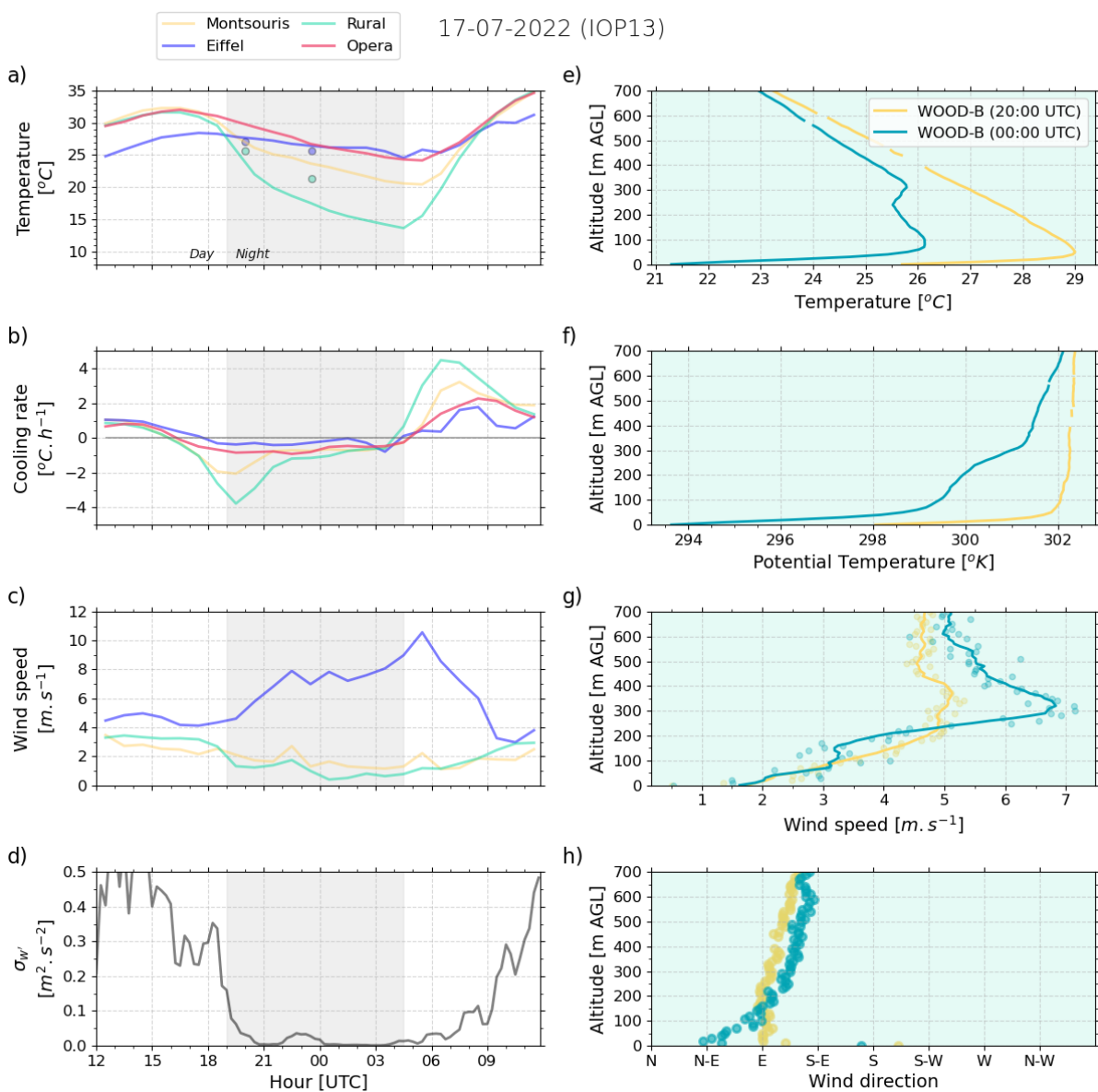
575

576



577

578 Figure 5: Time series and windsonde profile measurements for July 12, 2022. a-d) Time series
 579 measurements from 12 UTC to 12 UTC (D+1). a) Temperature at Montsouris Park, Rural
 580 settings, Opera (built-up) and top of Eiffel Tower. The coloured dots show the temperature
 581 measured by windsonds at 16, 20, and 00 UTC, respectively at park level and at the height of
 582 the Eiffel Tower (287m AGL). b) Cooling rate at Montsouris, Rural, Opera and Eiffel Tower. c)
 583 Wind speed at Montsouris, Rural, and Eiffel Tower. d) Vertical velocity variance from DWL at
 584 240 m AGL at QUALAIR-SU site. e-h) Vertical profiles from radiosonde measurements
 585 released in PARK-E at 16, 20, and 00 UTC, respectively. e) Temperature profile. f) Potential
 586 temperature profiles. g) Wind speed profiles. h) Wind direction profiles.
 587



588
 589 Figure 6: same as Fig. 5 for July 17, 2022.

590
 591

592
593
594
595
596
597
598
599
600

601 4.2 Intermediary regime: moderate park cooling effect 602 combined with strong UHI intensity

603

604 The evening of 15-16/07, compared to those discussed in Section 4.1, is characterised by
605 weaker cooling between 16 and 00 UTC in the rural setting and urban park, and stronger
606 cooling in the built-up environment, as shown in Table 2. It is classified in the intermediary
607 regime. Cooling peaks near $-3^{\circ}\text{C}/\text{hr}$ in the rural setting and $-1.5^{\circ}\text{C}/\text{hr}$ in urban park, which is
608 slightly less than for the cases of Section 4.1 (Fig. 7b). For this regime, the nocturnal near-
609 surface wind only decreases in the rural setting while it increases in the urban park after 21
610 UTC as the wind aloft picks up (Fig. 7c) which indicates that vertical momentum transfer is
611 less inhibited above the urban surface. Figure 7d shows that the vertical turbulent mixing
612 remains above $0.1 \text{ m}^2 \text{ s}^{-2}$ after sunset and increases to $0.2 \text{ m}^2 \text{ s}^{-2}$ during the evening which
613 confirms that the UBL remains turbulent during the night.

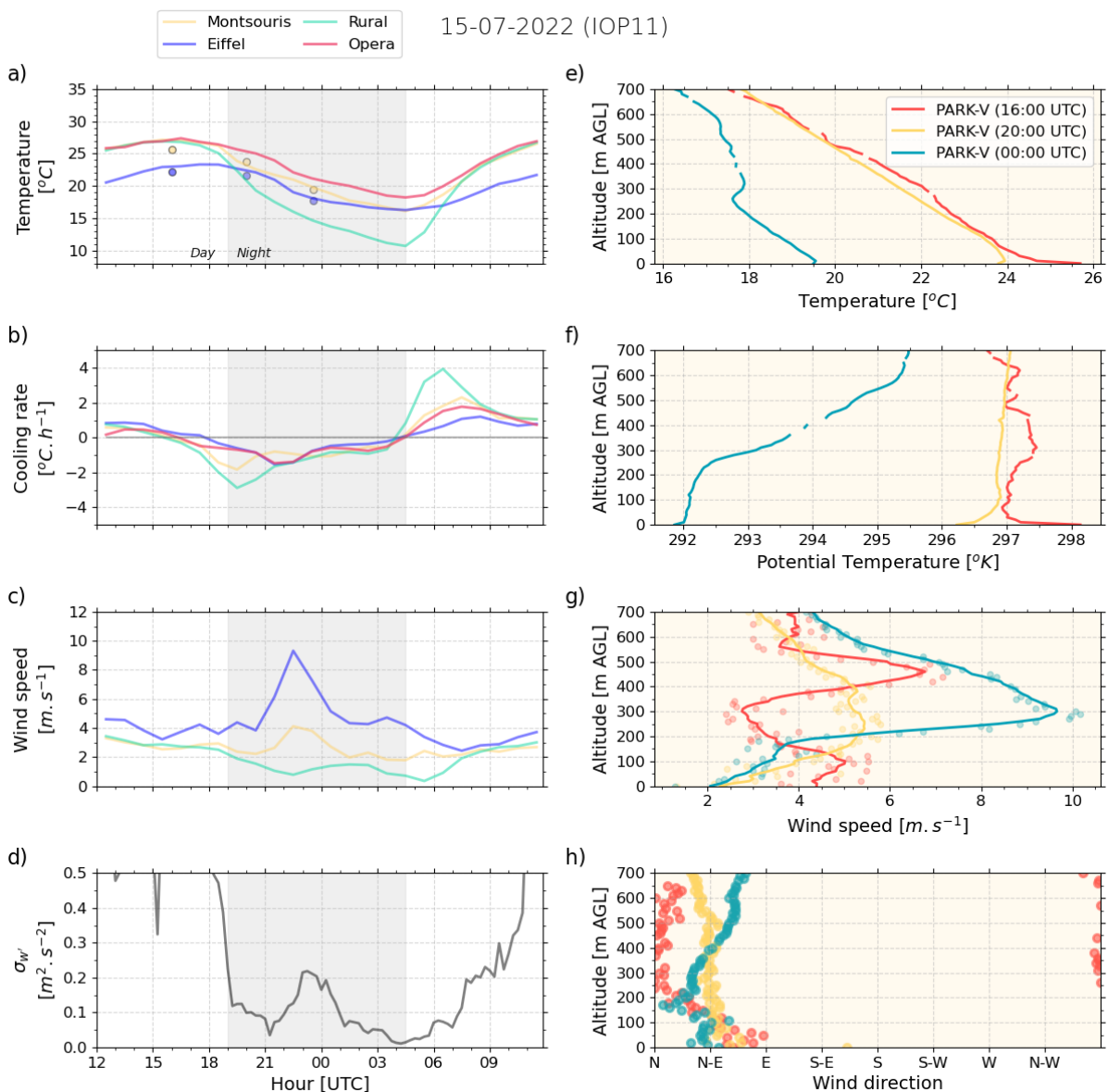
614

615 The windsound profiles carried out in the La Villette urban park (PARK-V on Fig. 1), for which
616 the vegetated area is comparable to that of the Montsouris urban park, reveal at 20 UTC a
617 slight surface-based inversion with a neutral layer above, while at 00 UTC under brisker
618 turbulent mixing the UBL remains near-neutral from the ground up to a temperature
619 inversion near 300 m AGL. It is then likely that the UBL remains neutral due to sensible heat
620 flux originating from the hot surface combined with turbulent mixing and from the
621 temperature inversion above. Again, a clear low-level jet with peak horizontal velocity $> 9 \text{ m}$

622 s^{-1} near the height of the temperature inversion suggests that stably stratified air from rural
 623 surroundings is advected over the city.

624
 625 The intermediary regime highlights that while the rural nocturnal layer becomes statically
 626 stable during the evening, as evidenced by the very low near-surface wind speed at the rural
 627 site, the UBL remains statically neutral. Vertical turbulent mixing in the UBL prevents a
 628 temperature inversion to form in the UCL, even above the urban green space.

629



630
 631 Figure 7: same as Fig. 5 for July 15, 2022 (IOP11)

632
 633

634
635
636
637
638

639 4.3 Turbulent regime: weak park cooling effect combined with 640 weak regional UHI intensity

641

642 The evening of 04/07, classified in the turbulent regime, is characterised by nearly identical
643 cooling rates in built-up settings, urban green spaces, as well as aloft at the top of the Eiffel
644 Tower. Cooling peaks near -2 to -2.5°C/hr at all locations (Fig. 8b). Wind speed at both the
645 rural settings and the urban park does not decrease after sunset, but rather increases after
646 18 UTC as the wind aloft picks up (Fig. 8c). In addition to the strong advection effects, the UBL
647 remains turbulent during the night as turbulent vertical mixing remains above $0.2 \text{ m}^2\text{s}^{-2}$ after
648 sunset (Figure 8d), both indicating that vertical momentum transfer is not inhibited across the
649 region.

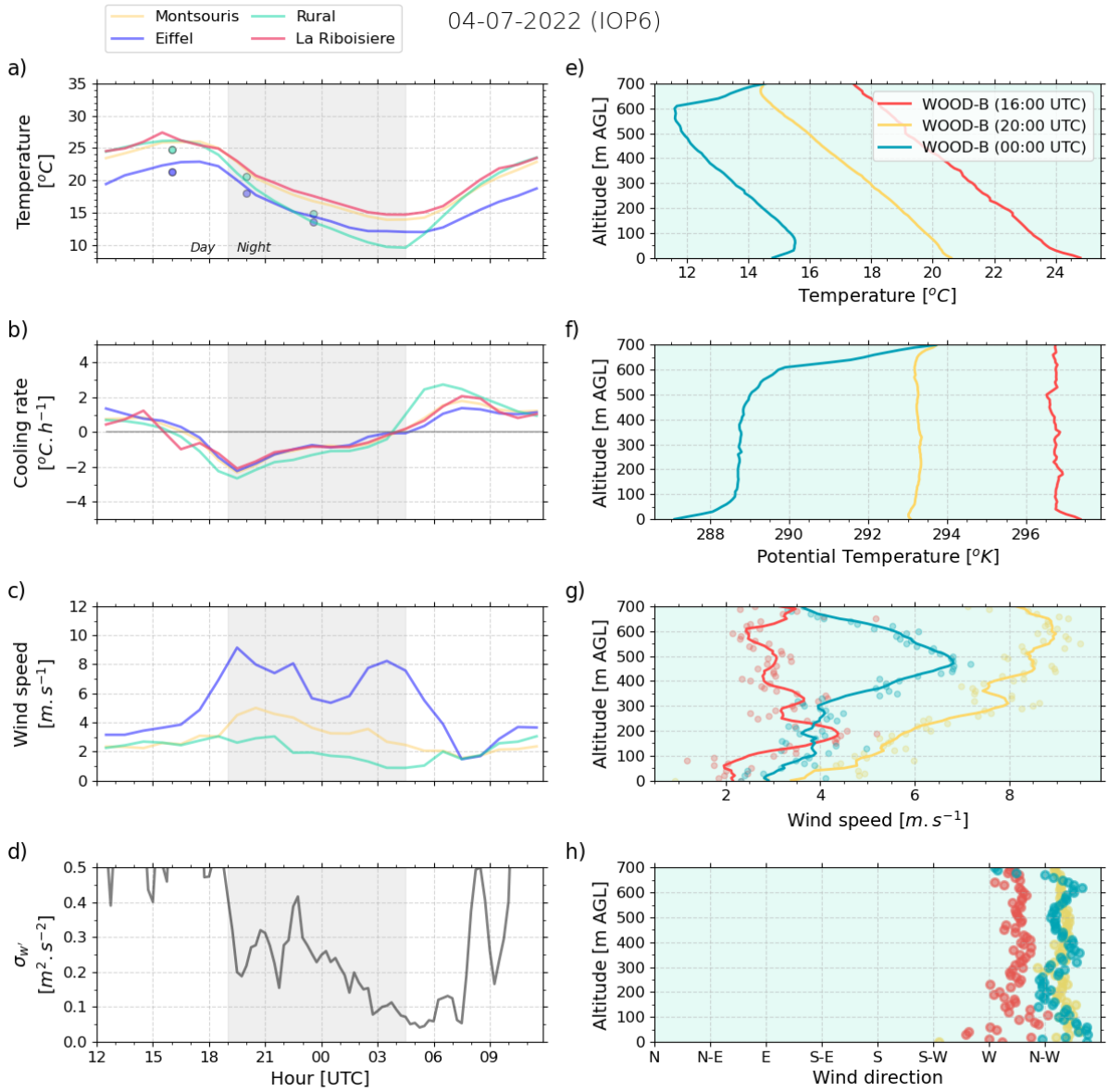
650

651 The windsound profiles carried out at the Bois de Boulogne large urban wood (WOOD-B in Fig.
652 1), detected a neutral UBL from 0 to 700 m AGL at 20 UTC. At 00 UTC, under continued brisk
653 turbulent mixing, a weak 1°C temperature inversion forms over the large green space while
654 the neutral UBL extends from 100m to 600 m AGL and is capped by a 5°C temperature
655 inversion.

656

657

658



659

660 Figure 8: same as Fig. 5 for July 04, 2022

661

662

663

664

665

666

667

668

669

670 5 - Characteristics and impacts of turbulence 671 regimes

672

673 To better understand the impact of wind, turbulence and static stability on differential cooling
674 between built-up areas, urban parks and rural settings, we analyse the characteristics of the
675 three turbulence regimes encountered during summer 2022. First, we study the diurnal
676 evolution of wind and turbulence in built-up settings, urban green spaces and rural
677 surroundings (Section 5.1) and then investigate the atmospheric static stability in the built-up
678 surfaces and green infrastructures (Section 5.2) for the three regimes. Finally, we analyse the
679 diurnal cycle of temperature and discuss the nocturnal cooling in built-up environments,
680 green infrastructures and rural settings for the three regimes (Section 5.3).

681 5.1 Wind and turbulent mixing characteristics of turbulence 682 regimes

683 First, we study how wind speed evolves at diurnal scales over the city (Montsouris urban
684 park), in the rural setting (Melun), and aloft (top of Eiffel Tower) for the turbulence regimes
685 identified in Section 3 (Fig. 9).

686

687 In the stagnant regime (highest UHI intensity and lowest vertical velocity variance), we find
688 that at sunset, when vertical mixing drops, the wind speed aloft increases while the near-
689 surface wind speed decreases both over the urban park and in the rural setting (Fig. 9a).
690 Vertical velocity variance reaches values below $0.05 \text{ m}^2 \text{ s}^{-2}$ shortly after sunset. Not only the
691 rural nocturnal boundary layer but also the UBL becomes stratified, thereby inhibiting vertical
692 transfer of momentum. The stable UBL becomes decoupled from the neutral layer above,
693 allowing near-surface wind speeds to decrease, on average below 2 m s^{-1} , through surface
694 drag, while wind speed aloft experiences reduced friction and hence increases.

695

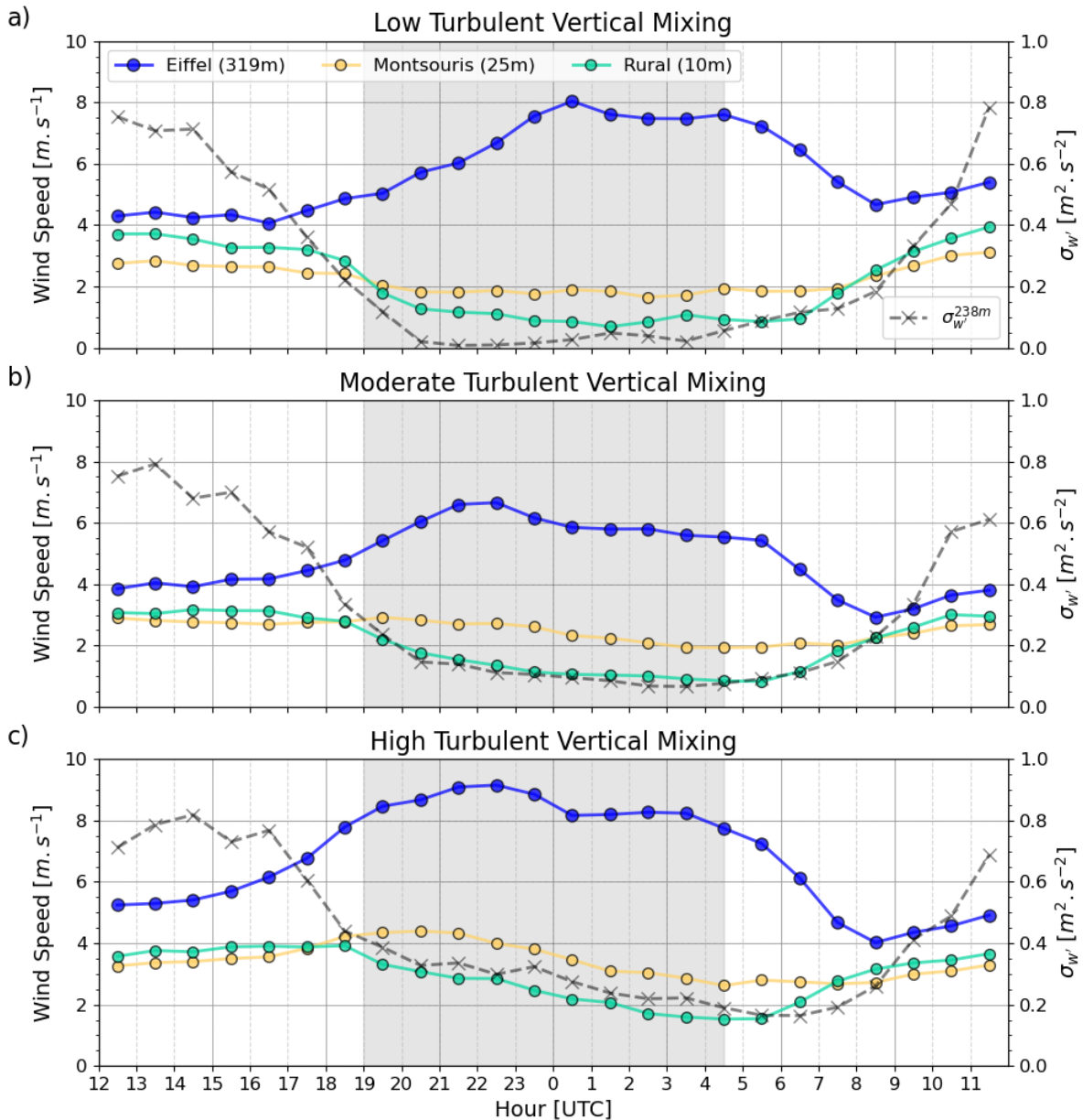
696 In the intermediate regime (strong ΔUHI and moderate vertical velocity variance), we observe
697 that on average, the vertical velocity variance decreases later than in the stagnant regime and
698 it is 50 % stronger at sunset, reaching $0.15 \text{ m}^2 \text{ s}^{-2}$ on average during the night (Fig. 9b). The

699 near-surface wind speed in the rural setting decreases at sunset similarly to the stagnant
700 regime, so we can hypothesise that the atmosphere becomes stable in the rural environment.
701 In the urban green spaces, the near-surface wind speed remains unchanged after sunset,
702 which is consistent with a continued vertical transfer of momentum. Still, the stable
703 stratification over the rural area tends to favour the formation of a low-level jet, a
704 phenomenon that occurs in Paris in 70% of the nights in summer 2022 (Cespedes et al. 2024),
705 so that the wind speed above the neutral UBL can double in magnitude between noon and
706 midnight.

707

708 In the turbulent regime (low UHI intensity and high vertical velocity variance) vertical velocity
709 variance in the UBL is on average above $0.3 \text{ m}^2 \text{ s}^{-2}$ at sunset (Fig. 9c). Near-surface wind speed
710 in the rural setting remains above 3 m s^{-1} on average, while central urban wind speeds
711 increase consistently across the UBL, i.e. both near the surface and at the top of the Eiffel
712 Tower.

713



714

715 Figure 9 : Average diurnal cycles over summer 2022 for each of the turbulence regimes
 716 (stagnant at the top, intermediary in the middle, and turbulent at the bottom): wind speed
 717 measured at Melun (rural site); Montsouris park (urban park); top of Eiffel Tower; and vertical
 718 velocity variance at 240 m AGL derived from Doppler Lidar measurements.

719 5.2 Atmospheric stability characteristics of turbulence regimes

720

721 In Section 4, we found evidence that the static stability above urban parks and urban woods
 722 can vary significantly depending on the turbulent vertical mixing in the UBL. To study this
 723 variability, we derive the potential temperature lapse rates for each windsound profile carried

724 out at 20 and 00 UTC above urban woods and parks, as well as radiosonde profiles launched
725 at the same time from the built-up area of Bercy (URBAN-B location on Fig. 1) along the Seine
726 river, and plot them against the vertical velocity variance estimated from the DWL
727 measurements at the same time (Fig. 10). The potential temperature lapse rate is derived for
728 two vertical intervals, 0-50 m AGL representing the height over which surface-based
729 inversions are typically observed (also called park/wood internal boundary layer), and 100-
730 200 m AGL representing the nocturnal UBL. Vertical velocity variances shown in Fig. 10 are
731 one-hour average values. The turbulence regime derived for each evening (19-02 UTC) is also
732 shown. Fig. 10b reveals that, when the vertical velocity variance drops below $0.05 \text{ m}^2 \text{ s}^{-2}$
733 (corresponding mostly to the stagnant regime) the near-surface potential temperature lapse
734 rate above urban parks (about 20 ha) ranges $4\text{-}6^\circ\text{C}/100 \text{ m}$ while those above the woods (about
735 900 ha) can reach $8\text{-}14^\circ\text{C}/100 \text{ m}$. In the lowest vertical velocity variance conditions (< 0.025
736 $\text{m}^2 \text{ s}^{-2}$), near-surface potential temperature lapse rates in built-up areas also become positive
737 ranging $1\text{-}3^\circ\text{C}/100 \text{ m}$. This confirms that stable stratification can occur in all settings, but the
738 strength of the stratification depends on the surface type.

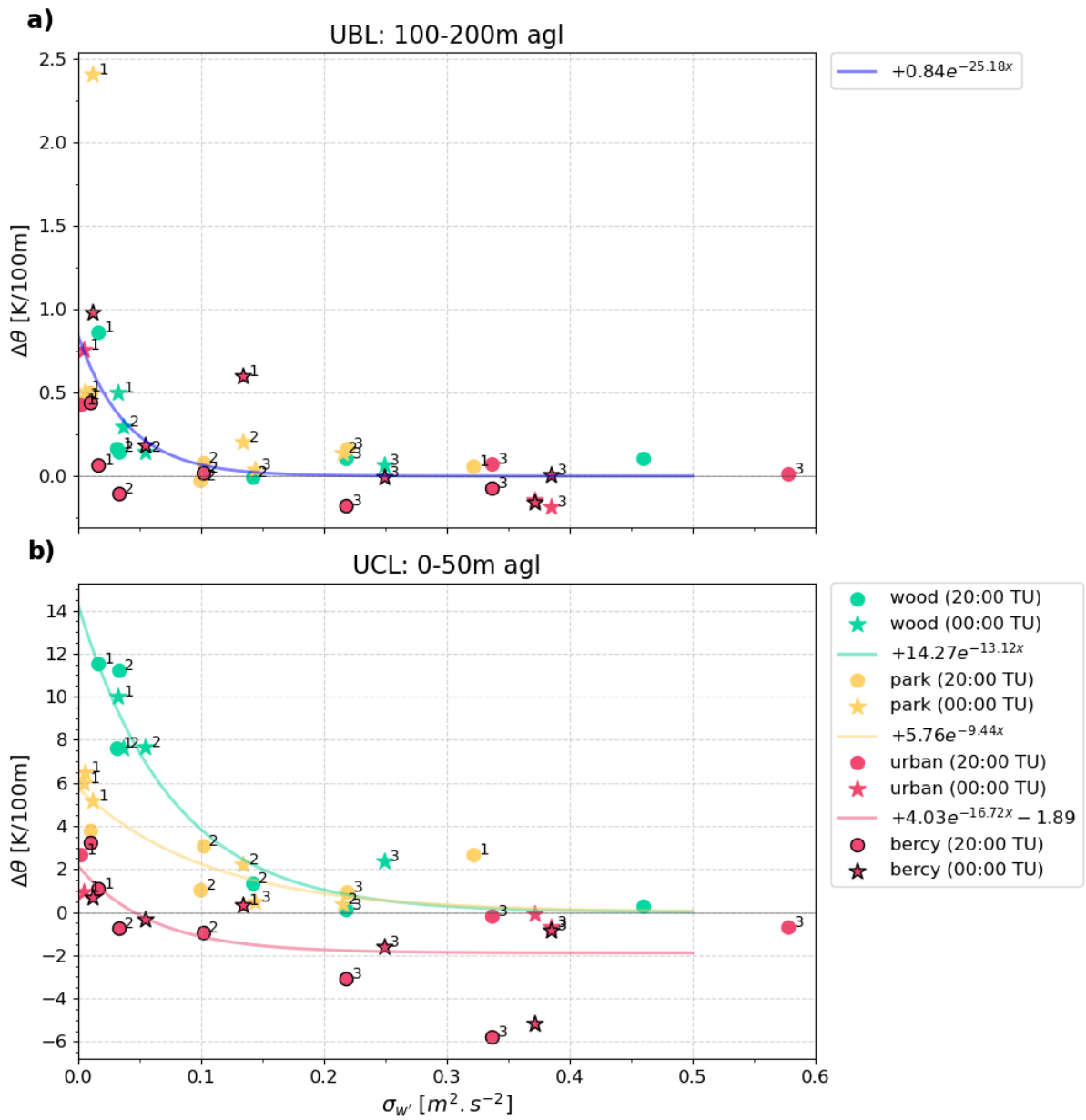
739 For vertical velocity variances ranging $0.1\text{-}0.2 \text{ m}^2 \text{ s}^{-2}$, near-surface potential temperature lapse
740 rates above parks and woods range between $0\text{-}3^\circ\text{C}/100 \text{ m}$, decreasing to near adiabatic
741 conditions ($0^\circ\text{C}/100 \text{ m}$) as turbulent mixing increases. In built-up areas, we find that near-
742 surface potential temperature lapse rates become negative (near $-1^\circ\text{C}/100 \text{ m}$) as soon as the
743 vertical velocity variance exceeds $0.05 \text{ m}^2 \text{ s}^{-2}$, a signature of a typical unstable urban surface
744 layer.

745 This analysis provides quantitative evidence that evening and night-time air temperature
746 conditions in the UCL become spatially heterogeneous when turbulent mixing in the UBL is
747 very weak. Only then it is possible for a strong temperature inversion to form over the urban
748 green space through the support of radiative flux divergence. The cool air remains in a local,
749 internal park/wood thermal boundary layer and does not mix with the relatively warm air in
750 the surrounding neighbourhoods. The significance and vertical extent of this cool air pool
751 increases with green space size, and it can be speculated that also green fraction and soil
752 moisture levels would enhance the effect.

753

754 The turbulent mixing in the UBL varies with the static stability of the UBL. As shown in Fig.
755 10a, when the potential temperature lapse rate at 100-200 m AGL increases to values near

756 +0.5°C/100m for all settings, including built-up areas, the vertical velocity variance decreases
 757 below 0.05 m² s⁻². No clear contrast in stability is found above the different surfaces,
 758 confirming that under the stagnant regime, the nighttime UBL is very shallow.
 759



760

761 Figure 10: Nighttime (20 and 00 UTC) potential temperature lapse rate above wood (green),
762 park (orange) and built-up areas (red) as a function of σ_w in the UBL (at 240 m AGL) for (a) a
763 layer between 100-200 m AGL and (b) a layer between 0-50 m AGL. Symbols indicate time
764 UTC. Urban labels with black borders correspond to data from radiosoundings launched from
765 the URBAN-B site and the others to data from windsonds (various sites). The number shows
766 the mean evening (19-02 UTC) turbulence regime for each case.

767

768 5.3 Impact of turbulence regimes on diurnal temperature 769 evolution

770

771 Ultimately, we want to determine how the turbulence regimes can impact the nocturnal
772 cooling provided by urban green infrastructures. Figure 11 shows the mean diurnal cycles of
773 temperature for stagnant, intermediary and turbulent regimes (a, b, and c, respectively). The
774 temperature diurnal cycles are normalised by subtracting the temperature measured at 16
775 UTC (peak daytime temperature). On average, daytime peak temperatures are highest for the
776 stagnant regime near 31°C, while they peak at about 27°C for the other two regimes. Figure
777 11 shows that after 16 UTC, the temperature at all sites decreases to a minimal value by the
778 next morning at sunrise. In 12 hours, the temperatures drop between 8 and more than 14°C
779 depending on the surface type and the turbulence regime. The stagnant regime reveals the
780 strongest contrasts between the settings (Fig. 11a). At 00 UTC, five hours after sunset, the
781 built-up neighbourhood cooled by 5.5°C, while the urban park cooled by 9.0°C and the rural
782 sites by almost 13.8°C. This confirms earlier findings (Table 2 and Section 5.2) that under low
783 turbulent vertical mixing, the radiative cooling of the surface in urban park and rural settings
784 combined with low turbulent vertical mixing provides an efficient cooling of the near-surface
785 atmosphere. In such conditions, urban parks can provide significantly cooler conditions than
786 the built-up neighbourhoods nearby.

787 In the intermediary regime, the evening cooling rate in the built-up environment is slightly
788 larger than for the stagnant regime (-6.2°C at 00 UTC, Fig. 11b). In the urban park, the
789 increased UBL turbulent vertical mixing reduces the strength of the near-surface radiative flux
790 divergence. The evening cooling in the urban park is not as strong (-7.5°C at 00 UTC) as in the

791 stagnant regime. In the rural setting, the evening cooling is also reduced in the intermediary
792 regime (-11.7°C at 00 UTC) compared to the stagnant regime, revealing that turbulence is also
793 likely stronger in the rural nocturnal boundary layer.

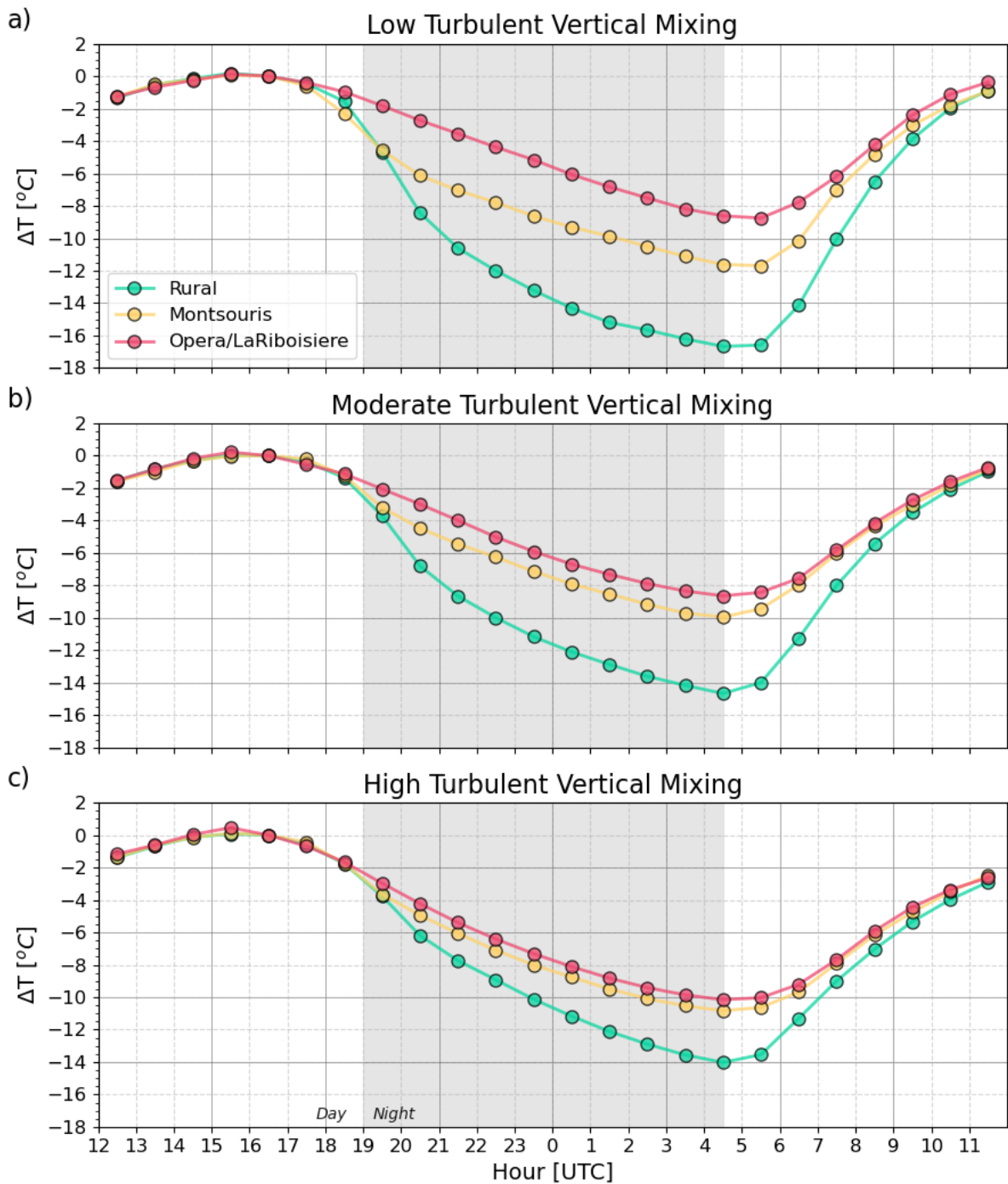
794 In the turbulent regime, with stronger turbulent vertical mixing and higher near-surface wind
795 speed than in the other regimes, the efficiency of the surface-driven cooling in the rural
796 setting is even more reduced, which limits the cooling compared to less turbulent conditions
797 (-10.6°C at 00 UTC, Fig. 11c). In the built-up environment, the air temperature drops by 7.6°C
798 between 16 and 00 UTC, i.e. 1.5-2°C more than in the other regimes. In this turbulent regime,
799 the city centre benefits from the cooling of the rural surroundings through advection – the
800 cooler air is mixed down into the UBL. In the urban park, two competing processes occur. The
801 radiative flux divergence is reduced by the strong mixing, but this again means cooler air
802 advected from rural surroundings is efficiently mixed down thereby contributing to a strong
803 cooling also in the urban park. Hence, we find that the temperature drops by 8.3°C on average
804 between 16 and 00 UTC, which is in between the stagnant and intermediary regime cooling.

805

806

807

808



809

810 Figure 11: diurnal cycle of temperature difference relative to the temperature at 16 UTC at
 811 Melun (rural site), Montsouris park (urban park) and Opera/Lariboisiere (Built-up setting) for
 812 stagnant, intermediary and turbulent regimes.

813

814

815 6) Conclusions

816 This study shows that the nocturnal cooling effect of urban parks depends on their
817 characteristics, such as their size, but also on UBL turbulent mixing and static stability regimes
818 that drive the relative importance of radiative and mixing transport cooling processes in the
819 UCL. We find that turbulent vertical mixing conditions measured by a Doppler Lidar at about
820 240 m AGL in the city centre are a very useful indicator to distinguish different evening cooling
821 regimes in the urban environment. These findings are summarised on a schematic (Fig. 12)
822 that represents, for each turbulent mixing regime, typical night-time vertical profiles of wind
823 and potential temperature above the urban environment and key processes that affect
824 nocturnal cooling.

825

826 Highest green space nocturnal cooling intensity occurs under stable stratification in the UBL
827 (statically stable, low turbulent mixing: vertical velocity variance of less than $0.05 \text{ m}^2 \text{ s}^{-2}$) over
828 both rural settings and urban parks. This stagnant regime is associated with large-scale
829 subsidence and large-scale advection of warm air aloft. The potential temperature profiles
830 above the urban parks and woods become statically stable soon after sunset due to radiative
831 cooling of the surface and subsequent cooling of the air by radiative flux divergence, in the
832 absence of a significant turbulent heat flux. A few hours after sunset, the entire UBL becomes
833 on average statically stable (about 200-250 m deep) due to subsidence and advection of the
834 stable rural air above the urban environment. Even if the heat release from the urban surface
835 would in theory lead to an unstable/near neutral urban boundary layer at night, we observe
836 that the strong stabilisation from above limits it strongly in height, or even totally inhibits it.
837 At the top of the UBL, a low-level jet develops over the night with peak wind speed, but
838 mechanical turbulence is inhibited by the static stability of the UBL. The advected rural air
839 mass remains stable above the urban environment because of unusually low vertical mixing
840 conditions. This stagnant regime exhibits the strongest evening cooling in both rural settings
841 and urban parks, and the weakest cooling in the built-up environment, hence strong nocturnal
842 temperature contrasts occur in the city depending on the vegetation fraction. In this regime,
843 the cooling effect of green infrastructure will depend on their size and likely on the vegetation
844 fraction of these areas. In this stagnant regime, we find comparable nocturnal cooling rates
845 (peaking at -2°C/hr around sunset) and static stability in the UCL (lapse rate near $6^\circ\text{C}/100\text{m}$

846 at 00 UTC) above the Montsouris park (15 ha) and the Eiffel tower park (24 ha) that are
847 roughly of the same size. Above urban woods (about 900 ha) near-surface lapse rates can
848 reach twice the value observed above urban parks (near 12°C/100m at 00 UTC). This leads to
849 the development of an internal UBL, about 50 m (100 m) deep, above urban parks (woods).

850

851 A second regime is identified, characterised by moderate turbulent vertical mixing in the UBL
852 (for vertical velocity variance between 0.1 and 0.2 m²s⁻²). Under this intermediary regime, the
853 potential temperature profiles above the urban park become neutral after sunset. A small
854 temperature inversion (<1°C above urban parks, <3°C above urban woods) can be found in
855 the UCL. A few hours after sunset, the UBL remains statically neutral up to 250-300 m due to
856 positive turbulent heat flux at the surface and at the top of the UBL which is characterised by
857 a temperature inversion. Advection of rural air brings a statically stable layer above the UBL.
858 Under this intermediary regime, the evening cooling in rural settings is about 2°C less than in
859 the stagnant regime. Two hours after sunset, the cooling in the urban park is also 2°C less
860 than in the stagnant regime, while the built-up environment is slightly cooler than in the
861 stagnant regime. There is probably vertical and also horizontal air mixing (advection or local
862 turbulence), which diminishes the cooling effect of small to medium-sized parks (15-25ha) by
863 mixing air from surrounding dense neighbourhoods. Hence, in the intermediary regime the
864 intra-urban temperature contrasts between areas with varying vegetation fractions are
865 significantly reduced.

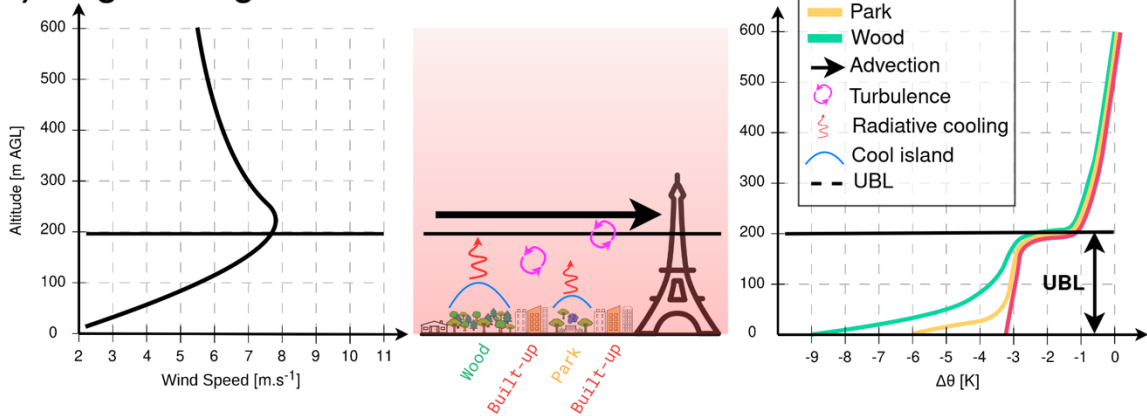
866

867 The third regime identified in this study results in the weakest nocturnal temperature
868 contrasts. Compared to the stagnant and intermediary regimes, the turbulent regime is
869 characterised by stronger advection and mesoscale circulation, wind shear and turbulent
870 vertical mixing. The UBL above the urban park becomes neutral after sunset, with a depth
871 that is significantly increased (>400 m) compared to the two other regimes. The UBL remains
872 neutral even several hours after sunset. In this turbulent regime, the evening cooling rates
873 are nearly identical in the built-up environment and in the urban parks. In this regime, high
874 turbulence and wind mix the air and homogenise temperatures at a larger scale (district-to-
875 city scale) than in the intermediary regime (neighbourhood scale), completely encompassing
876 and erasing the cooling effect of parks.

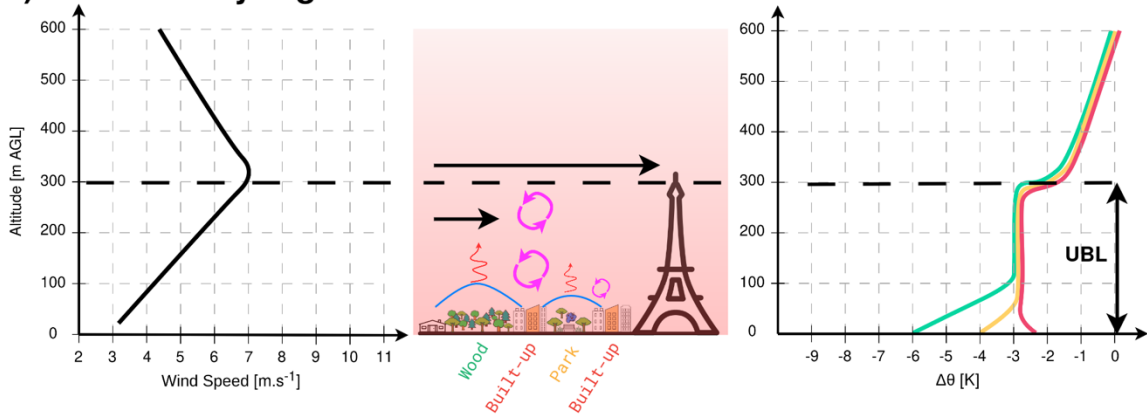
877

878 As statically stable low turbulent mixing conditions occur during the strongest heat waves due
879 to large-scale subsidence and advection of hot air, it is important to maintain spatially
880 distributed and accessible vegetated cool island spots in the city so that people can benefit
881 from cooler outdoor night-time conditions after being exposed to significant daytime heat
882 stress.
883

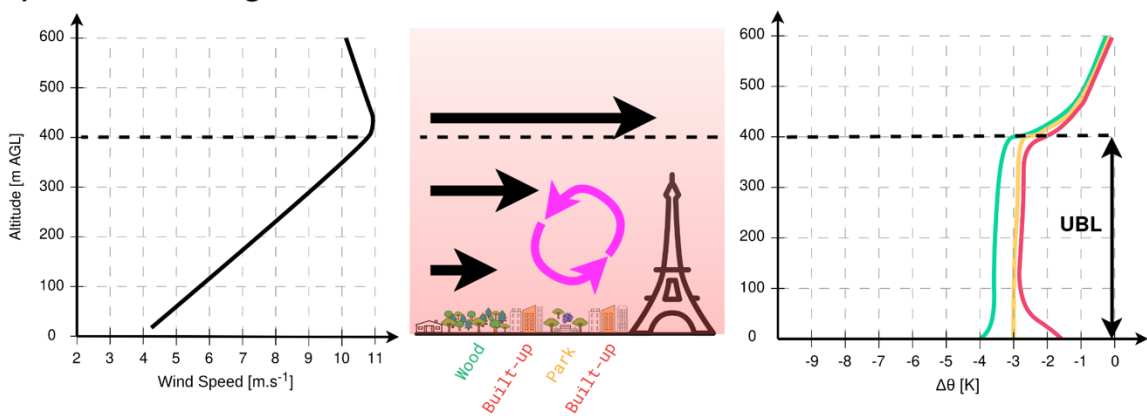
a) Stagnant regime



b) Intermediary regime



c) Turbulent regime



885

886 Figure 12. Typical night-time (near 00 UTC) vertical structure of wind speed (left) and
 887 potential temperature (right) in the urban boundary layer, observed during a)
 888 stagnant, b) intermediate, and c) turbulent mixing regimes. Potential temperature
 889 profiles are represented above built-up environments (red), urban parks (yellow) and
 890 urban woods (green). Key processes (advection, turbulent mixing, radiative cooling)
 891 affecting nocturnal cooling in the UBL are represented (centre).

892 Data availability

893 All raw data are available from the AERIS data centre catalogue at <https://paname.aeris->
894 [data.fr/data-catalogue-2/](https://paname.aeris-data.fr/data-catalogue-2/).

895

896 Author contributions

897 MH, SK, AL, and VM planned the campaign; MH, SK, JFR, JCD and JC performed the
898 measurements; MH, JFR, SK and JC analysed the data; MH and SK wrote the manuscript draft;
899 JFR produced the figures; AL, VM and TN reviewed and edited the manuscript.

900

901 Competing interests

902 The authors declare that they have no conflict of interest.

903

904 Acknowledgements

905

906 The PANAME experimental program benefited from several supports, including the research
907 project H2C funded by the French national agency for research (ANR) with the reference ANR-
908 20-CE22-0013, the Research Demonstration Project for Paris Olympics 2024 funded by
909 Météo-France and the Weather Meteorological Organization, the Paris Region PhD program
910 2020, investments from DIM QI2, OBS4CLIM-PIA3, CNRS-INSU and the ACTRIS research
911 infrastructure, and data management (AERIS national data and services center). The authors
912 would like to thank all the volunteers and participants who contributed to the success of the
913 SOP 2022, in particular the teams and many volunteers who carried out the windsonde
914 releases in the parks in the evening and at night and the radiosoundings at Bercy. Thanks are
915 extended to Hugo Ricketts for training the IPSL team to operate windsonds, with the support
916 of the European COST action PROBE. Authors would like to express their thanks to the
917 QUALAIR-SU scientific team who enabled the Doppler Lidar deployment on the site at

918 Sorbonne Université.

919

920 References

921 Aram, F. E. Higuera García, E. Solgi, S. Mansournia. Urban green space cooling effect in cities.

922 Heliyon 5 (2019) e01339. doi: [10.1016/j.heliyon.2019.e01339](https://doi.org/10.1016/j.heliyon.2019.e01339)

923 Barradas, V.L. Air temperature and humidity and human comfort index of some city parks of

924 Mexico City. *Int J Biometeorol* 35, 24–28 (1991). <https://doi.org/10.1007/BF01040959>

925

926 Rupa Basu, Jonathan M. Samet, Relation between Elevated Ambient Temperature and

927 Mortality: A Review of the Epidemiologic Evidence, *Epidemiologic Reviews*, Volume 24, Issue

928 2, December 2002, Pages 190–202, <https://doi.org/10.1093/epirev/mxf007>

929

930 Barthelmie, R. J., Grisogono, B., & Pryor, S. C. (1996). Observations and simulations of diurnal

931 cycles of near-surface wind speeds over land and sea. *Journal of Geophysical Research:*

932 *Atmospheres*, 101(D16), 21327-21337. <https://doi.org/10.1029/96JD01520>

933

934 Dahech, S., Charfi, S., & Madelin, M. (2020). Représentativité des températures mesurées

935 dans la station météorologique Paris-Montsouris. *Climatologie*, 17, 5.

936 <https://doi.org/10.1051/climat/202017005>

937

938 Bowler D. E., Lisette Buyung-Ali, Teri M. Knight, Andrew S. Pullin, Urban greening to cool

939 towns and cities: A systematic review of the empirical evidence, *Landscape and Urban*

940 *Planning*, Volume 97, Issue 3, 2010, Pages 147-155, ISSN 0169-2046,

941 <https://doi.org/10.1016/j.landurbplan.2010.05.006>

942

943 Cai, X., Yang, J., Zhang, Y. *et al.* Cooling island effect in urban parks from the perspective of

944 internal park landscape. *Humanit Soc Sci Commun* 10, 674 (2023).

945 <https://doi.org/10.1057/s41599-023-02209-5>

946

947 Chang C. C., Ming-Huang Li, Shyh-Dean Chang, A preliminary study on the local cool-island
948 intensity of Taipei city parks, *Landscape and Urban Planning*, Volume 80, Issue 4, 2007, Pages
949 386-395, ISSN 0169-2046, <https://doi.org/10.1016/j.landurbplan.2006.09.005>
950

951 Céspedes, J., Kotthaus, S., Preissler, J., Toupoint, C., Thobois, L., Drouin, M.-A., Dupont, J.-C.,
952 Fauchoux, A., and Haeffelin, M.: The Paris Low-Level Jet During PANAME 2022 and its Impact
953 on the Summertime Urban Heat Island, *EGUsphere* [preprint],
954 <https://doi.org/10.5194/egusphere-2024-520>, 2024.
955

956 Doick K. J., A. Peace, T. R. Hutchings, The role of one large greenspace in mitigating London's
957 nocturnal urban heat island, *Science of The Total Environment*, Volume 493, 2014, Pages 662-
958 671, ISSN 0048-9697, <https://doi.org/10.1016/j.scitotenv.2014.06.048>
959

960 Forceville G., A. Lemonsu, S. Gorla, M. Stempfelet, S. Host, J-M. Alessandrini, E. Cordeau, M.
961 Pascal, Spatial contrasts and temporal changes in fine-scale heat exposure and vulnerability
962 in the Paris region, *Science of The Total Environment*, Volume 906, 2024, 167476, ISSN 0048-
963 9697, <https://doi.org/10.1016/j.scitotenv.2023.167476>
964

965 Gao, Z., Zaitchik, B. F., Hou, Y., & Chen, W. (2022). Toward park design optimization to mitigate
966 the urban heat Island: Assessment of the cooling effect in five US cities. *Sustainable Cities and*
967 *Society*, 81, 103870. <https://doi.org/10.1016/j.scs.2022.103870>
968

969 Grimmond, C. S. B., and T. R. Oke, 2002: Turbulent Heat Fluxes in Urban Areas: Observations
970 and a Local-Scale Urban Meteorological Parameterization Scheme (LUMPS). *J. Appl. Meteor.*
971 *Climatol.*, 41, 792–810, [https://doi.org/10.1175/1520-
972 0450\(2002\)041<0792:THFIUA>2.0.CO;2](https://doi.org/10.1175/1520-0450(2002)041<0792:THFIUA>2.0.CO;2).
973

974 Haeffelin M, Barthès L, Bock O, Boitel C, Bony S, Bouniol D, Chepfer H, Chiriaco M, Cuesta J,
975 Delanoë J, Drobinski P, Dufresne J-L, Flamant C, Grall M, Hodzic A, Hourdin F, Lapouge F,
976 Lemaître Y, Mathieu A, Morille Y, Naud C, Noël V, O'Hirok W, Pelon J, Pietras C, Protat A,
977 Romand B, Scialom G, Vautard R (2005) SIRTa, a ground-based atmospheric observatory for
978 cloud and aerosol research. *Ann Geophys* 23:253–275, <https://doi.org/10.5194/angeo-23->

979 [253-2005](#).

980

981 Holmer, B., Thorsson, S., & Lindén, J. (2013). Evening evapotranspirative cooling in relation to
982 vegetation and urban geometry in the city of Ouagadougou, Burkina Faso. *International*
983 *Journal of Climatology*, 33(15), 3089-3105 , <https://doi.org/10.1002/joc.3561>.

984

985 Ibsen, P. C., Borowy, D., Dell, T., Greydanus, H., Gupta, N., Hondula, D. M., ... & Jenerette, G.
986 D. (2021). Greater aridity increases the magnitude of urban nighttime vegetation-derived air
987 cooling. *Environmental Research Letters*, 16(3), 034011, DOI 10.1088/1748-9326/abdf8a

988

989 Keatinge W R, Donaldson G C, Cordioli E, Martinelli M, Kunst A E, Mackenbach J P et al. Heat
990 related mortality in warm and cold regions of Europe: observational study *BMJ* 2000; 321 :670
991 doi:10.1136/bmj.321.7262.670

992

993 Laj, P., Lund Myhre, C., Riffault, V., Amiridis, V., Fuchs, H., Eleftheriadis, K., ... & Vana, M.
994 (2024). Aerosol, Clouds and Trace Gases Research Infrastructure–ACTRIS, the European
995 research infrastructure supporting atmospheric science. *Bulletin of the American*
996 *Meteorological Society*. <https://doi.org/10.1175/BAMS-D-23-0064.1>

997

998 Lemonsu, A., Belair, S. & Mailhot, J. The New Canadian Urban Modelling System: Evaluation
999 for Two Cases from the Joint Urban 2003 Oklahoma City Experiment. *Boundary-Layer*
1000 *Meteorol* 133, 47–70 (2009). <https://doi.org/10.1007/s10546-009-9414-2>

1001

1002 Lemonsu, A., V. Viguié, M. Daniel, V. Masson, Vulnerability to heat waves: Impact of urban
1003 expansion scenarios on urban heat island and heat stress in Paris (France), *Urban Climate*,
1004 Volume 14, Part 4, 2015, Pages 586-605, ISSN 2212-0955,
1005 <https://doi.org/10.1016/j.uclim.2015.10.007>.

1006

1007 Lemonsu, A., J.M. Alessandrini, J. Capo, M. Claeys, E. Cordeau, C. de Munck, S. Dahech, J.C.
1008 Dupont, F. Dugay, V. Dupuis, G. Forceville, S. Garrigou, O. Garrouste, M. Goret, S. Gorla, M.
1009 Haeffelin, S. Host, C. Joly, P. Keravec, S. Kotthaus, N. Laruelle, M. Madelin, V. Masson, C.
1010 Mauclair, T. Nagel, M. Pascal, J.F. Ribaud, G. Roberts, A. Rosso, A. Roy, M. Sabre, O. Sanchez,

1011 M. Stempfelet, W. Wei, R. Wilson, J. Wurtz, The heat and health in cities (H2C) project to
1012 support the prevention of extreme heat in cities, *Climate Services*, 2024, 100472, ISSN 2405-
1013 8807, <https://doi.org/10.1016/j.cliser.2024.100472>
1014

1015 Lemonsu A., Barrau S., Capo J., Céspedes J., Dahech S., de Munck C., Dumas G., Dupont J.-C.,
1016 Dupuis V., Etienne J.-C., Garrouste O., Goret M., Haeffelin M., Keravec P., Kotthaus S., Madelin
1017 M., Martinet P., Masson V., Nagel T., Price J., Ribaud J.-F., Rivollet M., Roberts G., Roy A.,
1018 Unger, V., Wilson R., Wallois S., Wurtz J., Multi-scale study of urban-atmosphere interactions
1019 in the Paris region (France) in the framework of the PANAME experiment, *Bull. Am. Met. Soc.*
1020 Submitted 2024.

1021

1022 Lin, Y., C. Wang, J. Yan, J. Li, and S. He, 2022: Observation and Simulation of Low-Level Jet
1023 Impacts on 3D Urban Heat Islands in Beijing: A Case Study. *J. Atmos. Sci.*, 79, 2059–2073,
1024 <https://doi.org/10.1175/JAS-D-21-0245.1>.
1025

1026 Martilli, A., 2002: Numerical Study of Urban Impact on Boundary Layer Structure: Sensitivity
1027 to Wind Speed, Urban Morphology, and Rural Soil Moisture. *J. Appl. Meteor. Climatol.*, 41,
1028 1247–1266, [https://doi.org/10.1175/1520-0450\(2002\)041<1247:NSOUIO>2.0.CO;2](https://doi.org/10.1175/1520-0450(2002)041<1247:NSOUIO>2.0.CO;2).
1029

1030 Morris, C. J. G., I. Simmonds, and N. Plummer, 2001: Quantification of the Influences of Wind
1031 and Cloud on the Nocturnal Urban Heat Island of a Large City. *J. Appl. Meteor. Climatol.*, 40,
1032 169–182, [https://doi.org/10.1175/1520-0450\(2001\)040<0169:QOTIOW>2.0.CO;2](https://doi.org/10.1175/1520-0450(2001)040<0169:QOTIOW>2.0.CO;2).
1033

1034 Murage, Peninah; Hajat, Shakoor; Kovats, R. Sari. Effect of night-time temperatures on cause
1035 and age-specific mortality in London. *Environmental Epidemiology* 1(2):p e005, December
1036 2017. | DOI: 10.1097/EE9.0000000000000005
1037

1038 Oke, T. R. (1976). The distinction between canopy and boundary-layer urban heat islands.
1039 *Atmosphere*, 14(4), 268–277. <https://doi.org/10.1080/00046973.1976.9648422>
1040

1041 Oke, T.R. (1982), The energetic basis of the urban heat island. Q.J.R. Meteorol. Soc., 108: 1-
1042 24. <https://doi.org/10.1002/qj.49710845502>
1043
1044 Oke, T. Towards better scientific communication in urban climate. *Theor. Appl. Climatol.* 84,
1045 179–190 (2006). <https://doi.org/10.1007/s00704-005-0153-0>
1046
1047 Oke, T. R., Mills, G., Christen, A., & Voogt, J. A. (2017). Urban climates. Cambridge University
1048 Press.
1049
1050 Pirard P, Vandentorren S, Pascal M, Laaidi K, Le Tertre A, Cassadou S, Ledrans M. Summary of
1051 the mortality impact assessment of the 2003 heat wave in France. *Euro Surveill.*
1052 2005;10(7):pii=554. <https://doi.org/10.2807/esm.10.07.00554-en>
1053
1054 von Rohden, C., Sommer, M., Naebert, T., Motuz, V., & Dirksen, R. J. (2022). Laboratory
1055 characterisation of the radiation temperature error of radiosondes and its application to the
1056 GRUAN data processing for the Vaisala RS41. *Atmospheric Measurement Techniques*, 15(2),
1057 383-405.
1058
1059 Royé, Dominic; Sera, Francesco; Tobías, Aurelio; Lowe, Rachel; Gasparrini, Antonio; Pascal,
1060 Mathilde; de’Donato, Francesca; Nunes, Baltazar; Teixeira, Joao Paulo. Effects of Hot Nights
1061 on Mortality in Southern Europe. *Epidemiology* 32(4):p 487-498, July 2021. | DOI:
1062 10.1097/EDE.0000000000001359
1063
1064 Shashua-Bar, L., M.E. Hoffman, Vegetation as a climatic component in the design of an urban
1065 street: An empirical model for predicting the cooling effect of urban green areas with trees,
1066 *Energy and Buildings*, Volume 31, Issue 3, 2000, Pages 221-235, ISSN 0378-7788,
1067 [https://doi.org/10.1016/S0378-7788\(99\)00018-3](https://doi.org/10.1016/S0378-7788(99)00018-3)
1068
1069 Steeneveld, G. J., B. J. H. van de Wiel, and A. A. M. Holtslag, 2006: Modeling the Evolution of
1070 the Atmospheric Boundary Layer Coupled to the Land Surface for Three Contrasting Nights in
1071 CASES-99. *J. Atmos. Sci.*, 63, 920–935, <https://doi.org/10.1175/JAS3654.1>.
1072

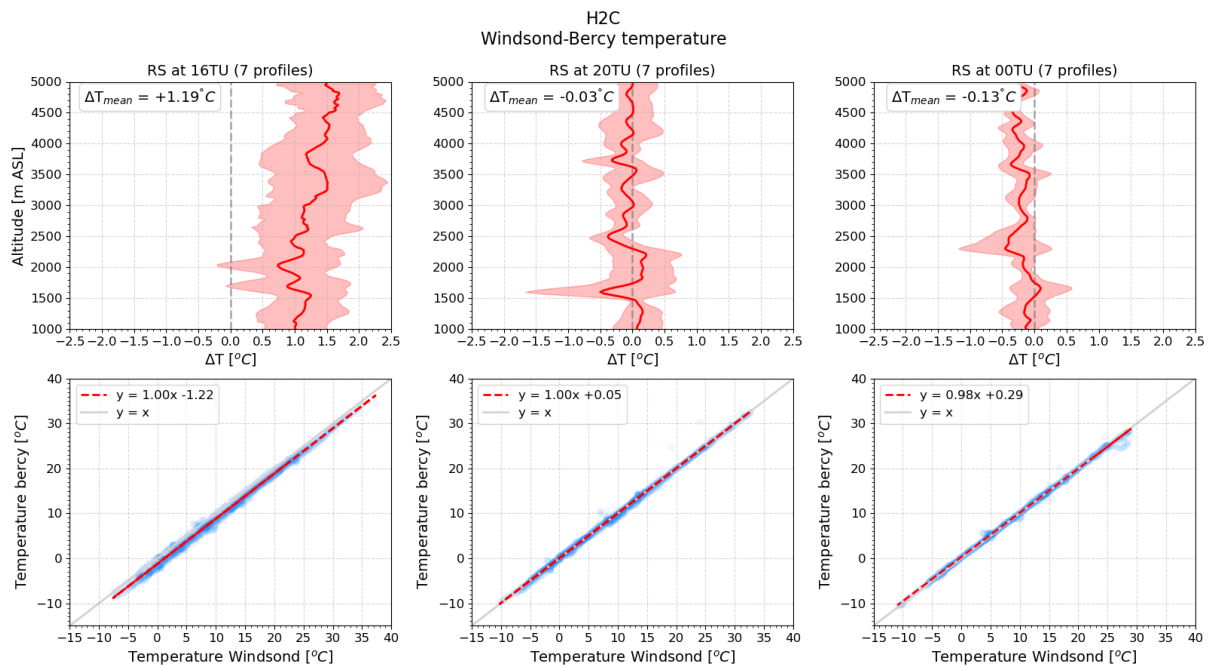
1073 Steeneveld, G. J., M. J. J. Wokke, C. D. Groot Zwaaftink, S. Pijlman, B. G. Heusinkveld, A. F. G.
1074 Jacobs, and A. A. M. Holtslag (2010), Observations of the radiation divergence in the surface
1075 layer and its implication for its parameterization in numerical weather prediction models, *J.*
1076 *Geophys. Res.*, 115, D06107, doi:[10.1029/2009JD013074](https://doi.org/10.1029/2009JD013074).
1077
1078 Taha, H., Akbari, H. & Rosenfeld, A. Heat island and oasis effects of vegetative canopies:
1079 Micro-meteorological field-measurements. *Theor Appl Climatol* 44, 123–138 (1991).
1080 <https://doi.org/10.1007/BF00867999>
1081
1082 Tsiringakis, A., Theeuwes, N.E., Barlow, J.F. *et al.* Interactions Between the Nocturnal Low-
1083 Level Jets and the Urban Boundary Layer: A Case Study over London. *Boundary-Layer*
1084 *Meteorol* **183**, 249–272 (2022). <https://doi.org/10.1007/s10546-021-00681-7>
1085
1086 Zhu, W.; Sun, J.; Yang, C.; Liu, M.; Xu, X.; Ji, C. How to Measure the Urban Park Cooling Island?
1087 A Perspective of Absolute and Relative Indicators Using Remote Sensing and Buffer Analysis.
1088 *Remote Sens.* 2021, *13*, 3154. <https://doi.org/10.3390/rs13163154>
1089
1090
1091
1092
1093

1094 **Appendix A: Windsond temperature profiles**
 1095 **assessment**

1096

1097 The evaluation of the Windsond temperature profiles was conducted by comparing them with
 1098 the Vaisala RS41 temperature profiles launched at Quai de Bercy (URBAN-B site in Fig. 1)
 1099 during the SOP 2022. Data from seven IOPs were used for this evaluation, with profiles
 1100 recorded at 16:00, 20:00, and 00:00 UTC, respectively. Von Rohden et al (2022) find a
 1101 radiation bias of 0.1°C in Vaisala RS41 temperature data in the troposphere. Our comparisons
 1102 reveal an average warm bias of 1.2°C in windsond temperature profiles compared to Vaisala
 1103 RS41 values of 16 UTC profiles. No significant bias is found at 20 and 00 UTC.

1104



1105

1106 Figure A1: Assessment of windsond temperature profiles. a-c) Average temperature
 1107 differences between the Windsond and Vaisala RS-41 temperature profiles from 1000m to
 1108 5000m ASL at 16, 20 and 00 UTC respectively. d-f) Point-to-point correlations between
 1109 Windsond and Vaisala RS-41 temperatures.

1110

1111

1112